Miner Deposita (2007) 42:639–662
DOI 10.1007/s00126-007-0133-7

ARTICLE

Carlin-type gold mineralization at Saint-André-de-Ristigouche, Gaspé Peninsula (Québec), Canadian Appalachians

V. Garnier · M. Malo · B. Dubé · A. Chagnon · G. Beaudoin

Received: 25 January 2006 / Accepted: 28 February 2007 / Published online: 28 March 2007

Abstract The Gaspé Peninsula, in the Canadian Appalachians, hosts a variety of mineral occurrences that are spatially associated with the Grand Pabos and Restigouche faults. Among these occurrences, the Saint-André-de-Ristigouche gold (SAR-Au) showing has peculiar features comparable with Carlin-type gold deposits at the regional, district, and prospect scales. The most striking ones are: (1) the calcareous nature of the host rocks; (2) the Au-As-Sb-Hg metallic signature with absence of base metals and Ag; (3) the association with a crustal scale fault zone; (4) the hydrothermal alteration characterized by silicification, calcite, and quartz veinlets at the margin of the Au-bearing zones and the occurrence of kaolinite in large halos of argillic alteration; (5) numerous felsic dikes; (6) the occurrence of Au in As-rich pyrite forming overgrowths on premineralization As-free pyrite, and in arsenopyrite; (7) hydrothermal fluids equilibrated with host rocks at high temperature (>200°), which cooled to precipitate arsenopyrite and then mixed with evolved meteoric water to precipitate stibnite in veins. Although the SAR-Au showing is relatively small, analogies with Carlin-type mineralization encourage exploration in the Gaspé Peninsula and in similar settings elsewhere in the Appalachians.

Keywords SAR-Au showing · Carlin-type deposits · Canadian Appalachians

Editorial handling: D. Lentz

V. Garnier · M. Malo (✉) · A. Chagnon
INRS-ETE,
490, rue de la Couronne,
Québec, QC, G1K 9A9, Canada
e-mail: mmalo@ete.inrs.ca

B. Dubé
Geological Survey of Canada - Québec,
490, rue de la Couronne,
Québec, QC, G1K 9A9, Canada

G. Beaudoin
Département de Géologie et Génie Géologique,
Faculté des Sciences et de Génie,
Université Laval,
Québec, Québec, G1K 7P4, Canada

Introduction

Major faults of the Canadian Appalachians host several types of gold mineralization (Gauthier et al. 1994; Swinden and Dunsworth 1995) including a variety of mineral occurrences that are spatially associated with the Grand Pabos and Restigouche faults in the Gaspé Peninsula (Fig. 1; Savard 1985; Malo et al. 1993). Polymetallic Cu-Pb-Zn-Ag-Au skarns and Au-bearing veins are the predominant styles of mineralization (Fig. 1). In addition, other mineral occurrences include serpentinite-hosted Ni–Cr occurrences, disseminated Zn-Pb-Cu-Ag and Ni occurrences in sandstone and mudstone, Cu occurrences in siltstone, and Pb–Zn occurrences in volcanic rocks (Savard 1985). Poulsen (1999a, b) suggested that geological environments, comparable to those hosting Carlin-type mineralization in Nevada, are present in southern Gaspé Peninsula (Québec) and in adjacent northwest New Brunswick. The metallogenic evolution of the Grand Pabos–Restigouche fault system was unravelled by detailed mapping (Malo et al. 1993), structural and paragenetic studies of skarns and Au-bearing veins (Chagnon 1984, 1988; Chagnon and Malo 1991; Malo et al. 1998), and lead isotopes data on galena (Moritz and Malo 1996). Malo et al. (1998, 2000) showed that the structural setting of the Saint-André-de-Ristigouche (SAR) gold showing, its metallic signature (Sb-Au-As±Hg), the nature of host rocks,

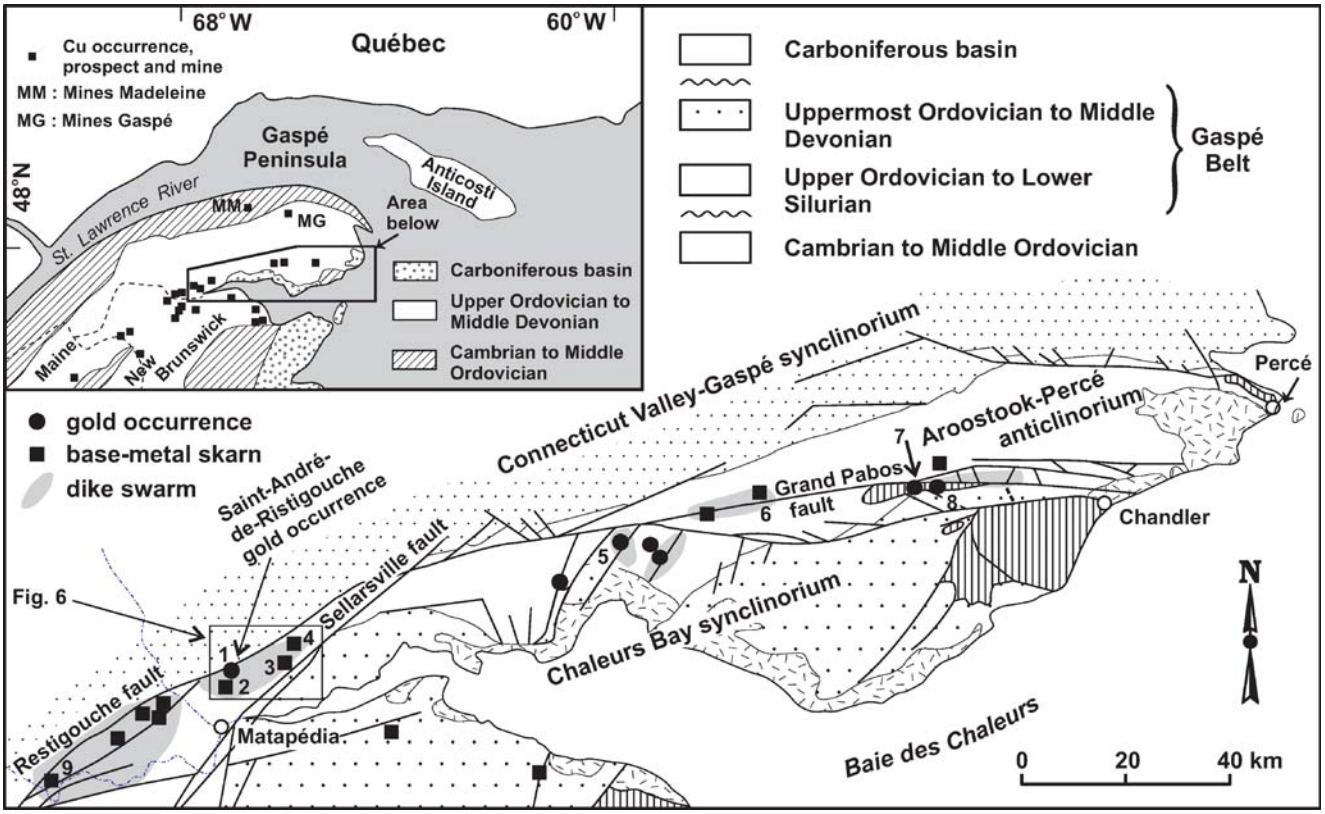

Fig. 1 Simplified geology of southern Gaspé Peninsula and location of the SAR-Au study area. Mineral occurrences: *1*, SAR-Au showing; *2*, Saint-André-de-Ristigouche Cu skarn; *3*, Basket Brook Cu–Ag skarn; *4*, Saint-Fidèle Cu skarn; *5*, Maria Au occurrence; *6*, Reboul base-metal skarn and Au occurrence; *7*, Lac Arsenault Au occurrence; *8*, Weir Au occurrence. *MG*, Mines Gaspé; *MM*, Mines Madeleine

and the presence of argillic alteration in the southwestern Gaspé Peninsula were regional features similar to those of the Carlin-type deposits region in Nevada.

This paper presents the petrographic, mineralogical, and geochemical characteristics of the mineralized rocks and Au-bearing minerals of the SAR-Au showing. To compare SAR-Au showing with Carlin-type gold deposits from Nevada, it is necessary to determine the nature of Au-bearing minerals, as Carlin-type deposits are characterized by rims of As-rich pyrite containing disseminated gold, overgrown on (As, Au)-free pyrite cores in silicified limestones.

The SAR-Au showing consists in two subvertical stibnite-quartz-Au fault-filled veins, surrounded by a halo of silicification developed within the host limestones. Our detailed petrographic and geochemical study shows that SAR-Au showing presents several of the main characteristics of Carlin-type deposits, and more particularly (As–Au)-rich pyrite rims on (As, Au)-free pyrite cores, which is a distinctive characteristic of Carlin-type gold deposits. Fluid inclusion microthermometric analysis and stable isotope geochemistry highlight the temperature and compositional properties of the mineralizing fluids and their interpreted sources. The results show that the SAR shares strong similarities with Carlin-type gold deposits from Nevada and represents the best example of this style of mineralization in the Gaspé Appalachians. In addition, new exploration targets are proposed, based on the structural, lithological and clay alteration features in the southwestern Gaspe Peninsula.

In this paper, the expression ‘Carlin-type’ gold deposits is prefered to ‘Carlin-like,’ as (1) ‘Carlin-like’ often refers to ‘distal-disseminated’ gold deposits (Berger and Bagby 1991; Tosdal 1999), (2) this study shows that the most important features characterizing Carlin-type gold deposits are found at SAR-Au showing, indicating that it is probably of Carlin affinity.

Geological setting

The Gaspé Appalachians in the Gaspé Peninsula is made up of Paleozoic rocks, mainly sedimentary with minor volcanic rocks, which can be divided into three temporal rock assemblages (Figs. 1 and 2): (1) Early Cambrian (Latest Precambrian?) to Late Ordovician rocks; (2) Late Ordovician to Middle Devonian rocks, the Gaspé Belt, and (3) Carboniferous rocks. The first rock assemblage was deformed by both the Taconian (Late Ordovician) and the Acadian (Middle Devonian) orogenies, whereas the second

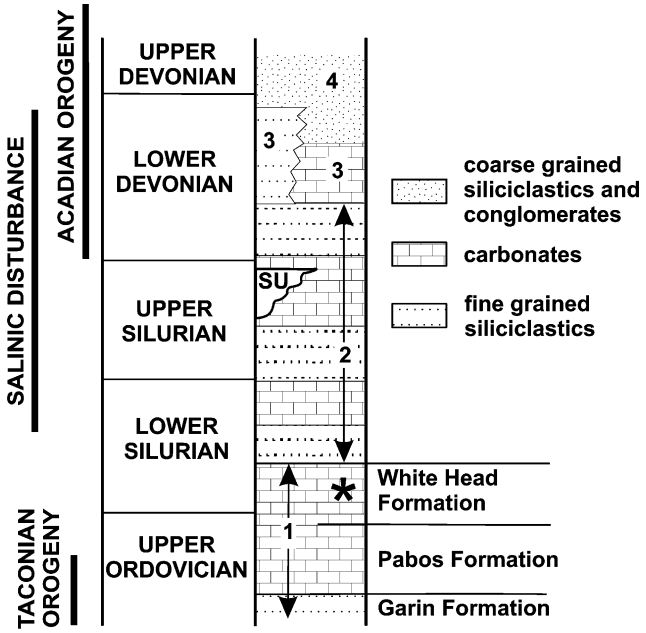

Fig. 2 Simplified stratigraphy of the study area adapted from Malo (2001). *1*: Honorat and Matapédia Groups; *2*: Chaleurs Group; *3*: Upper Gaspé Limestones and Fortin groups; *4*: Gaspé Sandstone Group; *SU*: Salinic unconformity

rock assemblage was deformed during the Acadian orogeny, but also recorded structural features linked to the Silurian Salinic disturbance (Malo and Kirkwood 1995; Malo et al. 1995; Malo 2001). Paleozoic rock assemblages remained largely unaffected by the Late Carboniferous-Permian Alleghanian orogeny.

Gaspé Belt stratigraphy

The southern Gaspé Peninsula contains the Upper Ordovician–Devonian rocks of the Gaspé Belt (Malo and Bourque 1993), which is divided into three major structural zones, from north to south: (1) the Connecticut Valley–Gaspé synclinorium; (2) the Aroostook–Percé anticlinorium, and (3) the Chaleurs Bay synclinorium (Fig. 1; Bourque et al. 2001). In the Québec segment, the stratigraphy in the Gaspé Belt is composed of four broad lithostratigraphic units (Fig. 2): (1) Upper Ordovician-lowest Silurian deep-water, fine-grained siliciclastic and carbonate facies (Honorat and Matapedia groups); (2) Silurian-lowest Devonian shallow to deep shelf facies (Chaleurs Group); (3) Lower Devonian mixed, fine-grained siliciclastic and carbonate facies (Upper Gaspé Limestones and Fortin groups); (4) upper Lower to Middle Devonian near-shore to terrestrial coarse-grained terrigeneous rocks (Gaspé Sandstones Group). Upper Silurian and Lower Devonian continental tholeiitic basalts and andesites occur in the upper part of the lithostratigraphic unit (2) and in lithostratigraphic units (3) and (4).

Rocks of the Gaspé Belt are bounded by two major angular unconformities. The oldest is between the Cambrian–Ordovician Taconian-deformed rocks and the base of the sequence, whereas the second is between the Acadian-deformed Gaspé Belt rocks and the overlying subhorizontal Carboniferous rocks. A Late Silurian unconformity, linked with Salinic synsedimentary block faulting, is recognized within the lithostratigraphic unit 2 (Fig. 2). The Gaspé Belt rocks were affected by regional anchi- to lower greenschist-grade (burial) regional metamorphism. Local zones of higher grade contact metamorphism are spatially associated with Devonian intrusions. Plutons are restricted to the northern part of the peninsula, whereas stocks and dike swarms are mainly emplaced along major Acadian faults (Doyon and Berger 1997), intrude the Gaspé Belt rocks further south (Fig. 1).

Structural setting

The Grand Pabos fault with its western extension, the Restigouche fault, and their subsidiary faults form a major Acadian dextral strike-slip fault system of the Gaspé Belt (Fig. 1). The Grand Pabos fault consists of a 100-m wide high-strain zone with ductile deformation (Kirkwood and Malo 1993). The Acadian regional structural trend of the Gaspé Belt rocks is northeast. Major east- to east/northeast-trending dextral strike-slip faults cut this trend (Fig. 1). Regional Acadian folds are generally open and upright. Near major faults, folds are tight, steeply plunging and inclined to the northwest or the southeast. A regional northeast-trending cleavage is well developed throughout the Gaspé Belt. Northeast-trending faults are high-angle reverse faults, northwesterly directed in the northern Gaspé Belt and southwesterly directed in the south (e.g., the Sellarsville fault in southwestern Gaspé Peninsula; Fig. 1). Salinic structural features are related to the Late Silurian extensional tectonics before contractional Middle Devonian Acadian folding and faulting. These features are mainly synsedimentary normal faults and extensional longitudinal folds (Malo 2001). Alleghanian orogeny is expressed only by minor normal faults in southern Gaspé Peninsula (Fig. 1).

Metallogeny

A number of gold prospects have been identified in the southern Gaspé Peninsula (Fig. 1). The most important are, from west to east: SAR, Maria, Reboul, Lac Arsenault, and Weir (Fig. 1). Twelve base-metal skarn prospects and occurrences are also known in this area (Fig. 1; Savard 1985). Rocks of the Aroostook–Percé anticlinorium, more particularly limestones of the White Head Formation (lithostratigraphic unit 1 of the Gaspé Belt), host these base-metal skarns, as well as the SAR gold prospect. Three

of these base-metal skarns are found in the vicinity of the SAR (Saint-André-de-Ristigouche Cu skarn, Basket Brook Cu–Ag skarn, and Saint-Fidèle Cu skarn, Fig. 1).

At the regional scale, the Restigouche fault is straight, but local releasing bends are present as typically found in large-scale strike-slip faults (Sylvester 1988). The SAR-Au showing is located at a releasing bend highly visible on a very low frequency electromagnetic anomaly map (Daigle 1990). Gold mineralization is mainly found in stibnite-quartz-Au veins trending N130°, compatible with local extension related to the overall dextral displacement along the Restigouche fault. The mineralized veins fill extensional fractures and exhibit open-space filling textures (Malo et al. 1998). Gold is also present in As-rich pyrite overgrowths on As-free pyrite cores in strongly silicified calcilutite.

Samples and analytical methods

The study area is about 18 km in length and 14 km wide in southwestern Gaspé Peninsula (Fig. 1). About 200 samples were collected from outcrops in creeks and along roads. In addition, more than 40 samples were collected in trenches at the SAR-Au showing from the main stibnite-quartz-Au vein and from altered limestones (Fig. 3). To better understand the geological context in which SAR-Au showing formed, and to define prospection guides, the alteration clay mineral assemblages were studied in a wider area including several Au and Cu prospects (Fig. 6).

Whole-rock analyses

Whole-rock analyses were done by SGS Minerals (Ontario, Canada). Samples were crushed to 2 mm and powered in a chrome steel mill to <75 μm. Major elements contents were determined by X-ray fluorescence spectrometry. Au contents were analyzed by Lead Fire Assay with gravimetric finish when exceeding 2,000 ppb, on 30-g samples. Hg was analyzed by cold vapour, and Te by hydride atomic absorbtion spectrometry. Other trace-element contents were determined by Induced Coupled Plasma Mass Spectrometry.

Clay mineralogy

The preparation of clay mineral concentrates was done at the INRS in Québec. Clay mineral concentrates were obtained by abrasion of rock fragments in demineralized water. The clay suspension was decarbonated in 1 N hydrochloric acid under constant agitation. The insoluble clay mineral residue was then separated by centrifuge into <2 μm and 2–16 μm granulometric fractions. X-ray diffraction analysis was performed on oriented mounts obtained by

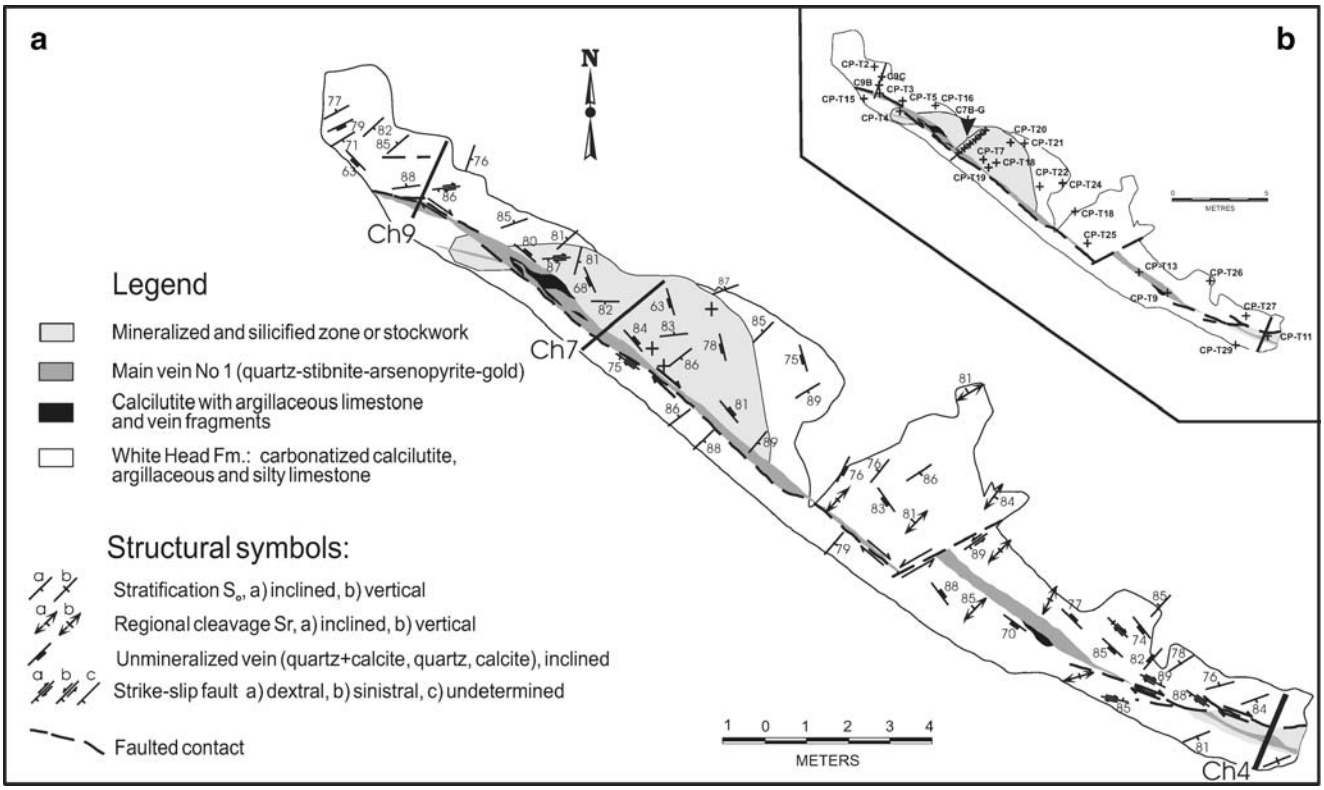

Fig. 3 Geology of the No.1 vein at SAR-Au showing. Modified from Pelchat (1995). *Ch4* and *Ch7* indicate the location of studied channel samples

sedimentation of clay suspensions onto glass slides, dried at room temperature, at Université Laval, Québec. Most samples were reanalyzed after saturation with glycerol. X-ray diffraction patterns were obtained on a Phillips diffractometer using CuK_{α} radiation at 40 kV and 20 mA, a goniometer speed of 2° 2θ/min, and digitalized and processed with the JADE software. The composition of illite and chlorite were evaluated by comparing the intensity ratios of their 002/001 and 004/003 reflections (Rey and Kübler 1983; Chagnon and Desjardins 1991).

Micro analytical techniques

Secondary electron and back-scattered electron images (BSE) were obtained with a JEOL-840-A Scanning Electron Microscope (SEM), and electron probe micro-analyses (EPMA) were performed using the Cameca SX100 of Université Laval, Québec. Pyrite and arsenopyrite crystals were analyzed by EPMA under acceleration voltage of 15 kV, a beam current of 40 nA and acquisition times of 20 and 10 s for Fe and S, respectively, whereas traces of Au, Sb and As were counted for 60, 40, and 30 s on peak with 20, 15, and 10 s on protolith (both sides). Natural and synthetic standards were used for calibration and data reduction was performed with PAP software (Pouchou and Pichoir 1991). The detection limits were 220 ppm for Au, 130 ppm for Sb, and 170 ppm for As.

Fluid inclusions

Microthermometry analyses were conducted on a US Geological Survey-style (Fluid) gas-flow heating and freezing stage calibrated with synthetic fluid inclusions. Ice-melting and homogenization temperatures are accurate and reproducible to ±0.2 and ±1°C, respectively. Fluid inclusions were studied using the fluid inclusion assemblages concept (Goldstein and Reynolds 1994). Criteria to identify inclusion origin included: (1) primary inclusions were identified by their presence on mineral growth zones; (2) secondary inclusions occur in planar arrays; (3) pseudosecondary inclusions occur in healed fractures that terminate within a crystal, and (4) all other inclusions were assigned an unknown origin.

Isotope geochemistry

Powdered samples of host-rock carbonates and vein calcite were obtained by micro drilling. The $\delta^{18}O$ and $\delta^{13}C$ values were determined at the Delta-Lab of the Geological Survey of Canada (Québec), following the method of Al-Aasm et al. (1990). $\delta^{18}O$ values of quartz were determined at the Stable isotope laboratory of University Laval (Québec) following the method of Clayton and Mayeda (1963). Data are reported in the usual 'per mil' (‰) notation relative to the standard Vienna Peedee belemnite (VPDB; C) and Vienna Standard Mean Ocean Water (VSMOW; O). Precision of data is always better than 0.1‰ for both $\delta^{18}O$ and $\delta^{13}C$ in carbonates and 0.2% in quartz. Accuracy is good, as determined by analysis of NBS-28 (quartz), NBS-18, NBS-19, CO1 and CO9 (carbonates).

Petrography of Au-Sb-As mineralization at SAR

The mineralization consists of two subvertical, Au-Sb-As-mineralized extensional quartz-carbonate-sulfide veins cutting across a meter-wide quartz±As-Sb-rich stockwork zone. They are hosted by Silurian laminated silty and argillaceous silicified limestone of the White Head Formation (Fig. 2). The main vein (No. 1; Fig. 3) is subvertical, 30 m long and 10–50 cm thick (Fig. 3; Wares 1990; Pelchat 1995). This vein averages 6.0 g/t Au (highest grade 39.6 g/t Au) and 2.43% Sb (Dessureault 1990). Vein No. 2 is located 75 m northeast of vein No. 1 and is 30 cm thick and 100 m long. It shows strong brecciation and consists of quartz, stibnite, and arsenopyrite hosted by argillaceous nonsilicified limestone (Dessureault 1990). All the data presented in this study come from vein No. 1.

Mineral paragenesis

The vein comprises 40–50% of drusy quartz (0.1–3 mm long), 10–15% of sparry calcite crystals, or millimetric to centimetric angular fragments of the host-rock, and 30–35% of sulfides, mostly stibnite with minor arsenopyrite and pyrite. Open spaces filling textures are locally present within the vein where 5–10-mm long quartz crystals are perpendicular to the walls. Prismatic stibnite crystals are 1–2 mm long and grew perpendicular to the vein wall and are usually better developed in the center of the vein. Arsenopyrite crystals are also perpendicular to the walls and are concentrated along the margins of the vein (Pelchat 1995). They represent 5% of the vein and occur as tabular aggregates up to 20 μm long, forming inclusions in quartz and stibnite. The host-rock fragments contain arsenopyrite and framboidal pyrite, probably of diagenetic origin. Dessureault (1990) reported gudmuntite (FeSbS) associated with stibnite, but it was not observed in this study. Kaolinite accounts for 1–2% of the vein. It fills interstices between quartz crystals, and it also occurs in limestone fragments.

The host limestone is silicified up to 2.5 m wide along the contact with the vein with locally massive silica replacement. A stockwork zone (1–2 m thick) of quartz-calcite veinlets is also developed in the host limestone. Most of the veinlets are northwest trending, subparallel to the main vein (Fig. 3), and the minor ones are northeast

trending, bedding parallel and perpendicular to the main vein (Fig. 3). Quartz crystals in northwest-trending veinlets are usually perpendicular to the walls. The silicified limestone contains up to 90% quartz with kaolinite, arsenopyrite, and pyrite (1–5%). Pyrite is mostly located along stratification planes in silty laminations. Within the silicified limestone, veinlets are made up of quartz. At a greater distance from the vein, silicification is less developed and the host rock suffered a late carbonatization. It is made up of 95% calcite, 2% quartz and 1% pyrite and arsenopyrite, with 5–10% of the carbonates in late calcite veinlets. In some samples, carbonate veinlets cut across quartz veinlets, clearly indicating that at least part of the carbonatization occurred after silicification. In addition, some veins show evidence of euhedral quartz crystals replaced by calcite. In both the silicified and carbonatized zones, pyrite is present as framboids and as idiomorphic grains. These idiomorphic grains may be of diagenetic or hydrothermal origin. Most of the idiomorphic grains are rimmed by arsenian pyrite (Fig. 4).

Careful SEM observations did not reveal the presence of microscopic gold grains in vein quartz and sulfides. EPMA shows that (1) Au is contained, in altered host rocks, in arsenian pyrite overgrowth on subidiomorphic pyrite; (2) in vein, Au is contained in arsenopyrite as well as in arsenian pyrite overgrowth on framboidal pyrite contained in host-rock fragments; and (3) the arsenian-rich overgrowths are also enriched in Sb. The paragenetic relationship among minerals is described in Fig. 5.

Hydrothermal clay mineral assemblages

X-ray diffraction analyses of insoluble residues from White Head limestones show that the mineralogical assemblages vary according to their proximity to faults or mineralized showings (Fig. 6). In addition to the unaltered clay assemblage, five alteration assemblages are defined by an index mineral or by abnormal proportions of illite or chlorite. The proportion of feldspar is variable and does not show any variation with other minerals or with the location of the sample.

Normal (protolith, unaltered) The less than 2 μm fraction of the unaltered or "normal" assemblage comprises the following: illite, chlorite, quartz, and rare Na-feldspar and/or K-feldspar. Illite and chlorite are well crystallized, illite to chlorite ratio is around 70:30. Kübler's illite crystallinity index (Kübler 1968) indicates anchi-epimetamorphic zones (Fig. 7). Moreover, peak intensity ratios indicate that illite belongs to the muscovite–phengite type and that chlorite is mainly magnesian (Chagnon 1988; Chagnon and Desjardins 1991). About 50% of the samples belong to this assemblage.

Illite assemblage This assemblage contains mainly illite with some quartz and sometimes traces of feldspar, chlorite and illite/smectite mixed-layer minerals. As seen in Esquevin's diagram (Fig. 7; Esquevin 1969), illite in this assemblage shows, generally, a more trioctahedral character than illite from other assemblages.

Kaolinite assemblage In this assemblage, kaolinite is accompanied by illite, quartz, and traces of feldspar. Only two occurrences of chlorite were observed in this assemblage. As shown by the 001/002 XRD reflection intensity ratio, the composition of illite is the same as in the unaltered assemblage (Esquevin's diagram; Fig. 7). However, some samples show a low 002/001 XRD reflection intensity ratio that is typical of the illite assemblage.

Smectite assemblage This assemblage contains illite as the major mineral with smectite and minor chlorite, quartz, and feldspar. The crystallinity of illite is similar to that of the unaltered assemblage.

Kaolinite + smectite assemblage Presence of both kaolinite and smectite characterizes this assemblage, where illite is always present with quartz and trace feldspar. Illite in this assemblage shows the crystallinity of illite in the unaltered assemblage.

Chlorite assemblage Chlorite is more abundant than illite. No other phyllosilicate is usually present. Quartz and rare feldspar are detected.

Distribution of the assemblages As shown in Fig. 6, the alteration assemblages form zoned halos or single spots. In the SAR area, two skarn zones are surrounded by zoned clay halos (1; Fig. 6). The skarn is characterized and surrounded by a chlorite zone assemblage that is in turn surrounded by smectite, kaolinite+smectite, kaolinite, and illite zones. The larger halo (1, 2; Fig. 6) is truncated by the Restigouche fault. Elsewhere, clay halos do not always contain all the assemblages. Eastward from the first two, a halo is found along the Restigouche fault without the skarn and the chlorite zone (3; Fig. 6). This is also the case in the southern part of the area along the Kempt West and Mill brooks (4; Fig. 6) and, further to the northeast, around the Basket Brook and St-Fidèle copper showings (5; Fig. 6). In this latter area, the chlorite assemblage is found, but skarn was not observed. Halos of clay mineral alteration assemblages are found adjacent or close to major faults. The SAR halo is crosscut by the Restigouche fault and no evidence for alteration is detected in rocks of the Fortin Group, north of the fault (Fig. 6; Duba and Williams-Jones 1983; Héroux and Chagnon 1986). Halos to the south are

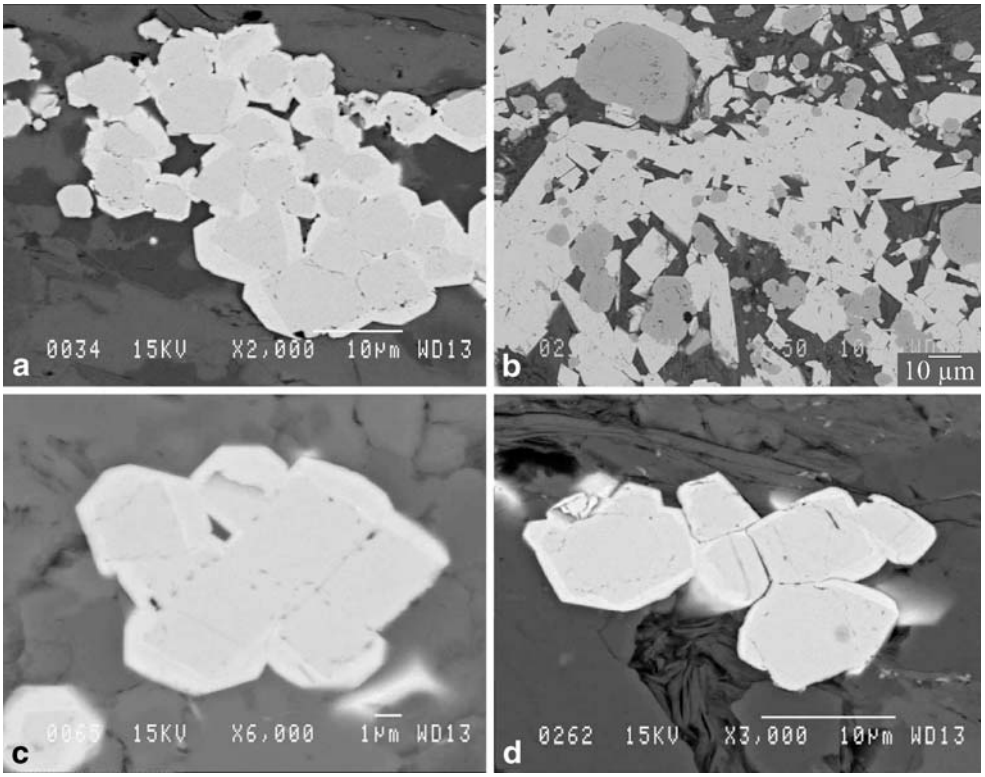

Fig. 4 **a**, **c**, **d** SEM-BSE images of pre-ore pyrite cores (*medium gray*) surrounded by arsenic- and gold-bearing overgrowths (*white*), in silicified calcilutite. Samples CP-T02-4, CP-T19, and CP-T18-4, respectively. **b** SEM-BSE images of pre-ore pyrite cores (*dark gray*) surrounded by arsenic- and gold-bearing overgrowths (*medium gray*) with arsenopyrite (*white*) in a calcilutite fragment contained in the main quartz vein (sample CP-T13-3)

located north of the Sellarsville fault and no sign of alteration was detected south of the fault (Fig. 6).

Alteration clay assemblages and mineralized showings

Four occurrences of copper mineralization are found in this area. All of them are associated with skarns and with the chlorite assemblage. The SAR-Au showing is found within the kaolinite assemblage, very close to the kaolinite-smectite assemblage.

Geochemistry

Whole-rock analyses

Major, minor, and trace element concentrations, in silicified and carbonatized rocks were determined to identify elemental gain/losses associated with mineralization and alteration (Tables 1 and 2; Fig. 3). Au is not only contained in the Au-Sb-quartz vein, but it is also present in the

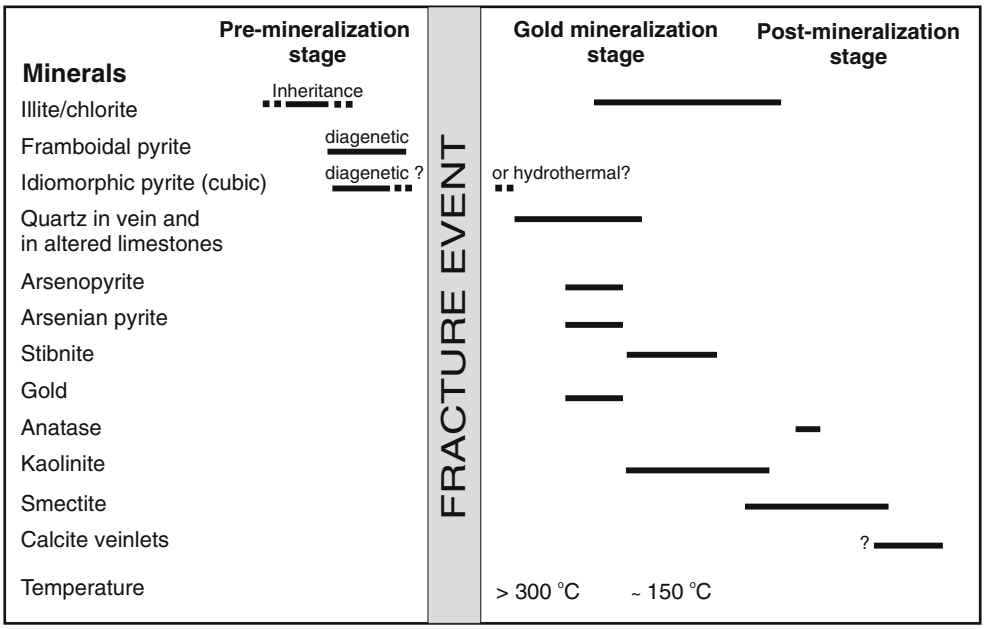

Fig. 5 Paragenesis of minerals in pre-, syn-, and post-gold mineralization stages

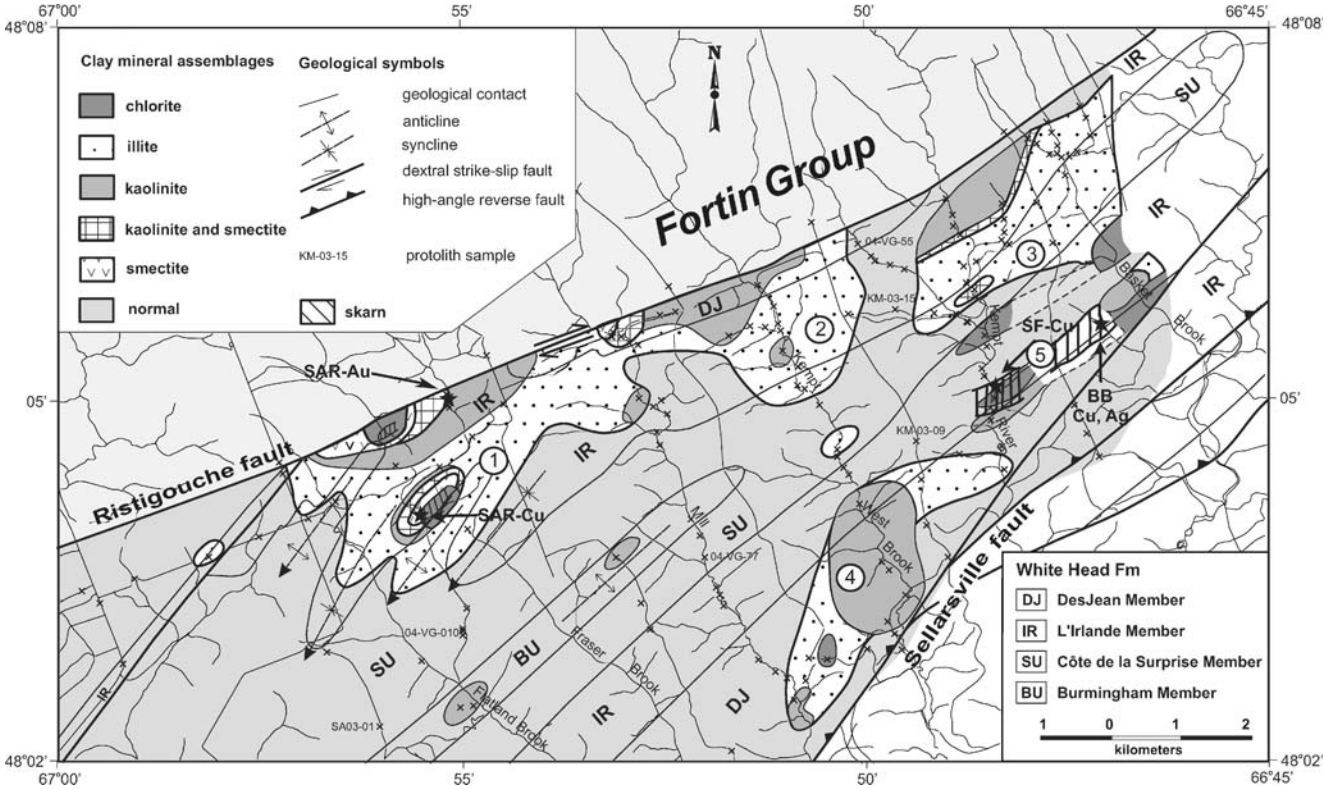

Fig. 6 Alteration map of southwestern Gaspé area near the SAR-Au showing based on clay mineral assemblages (modified from Chagnon 1984). *Crosses* correspond to the samples collected during summers 2003 and 2004. *BB, Cu–Ag* indicate Basket Brook Cu–Ag showing; *SAR-Au* indicate Saint-André-de-Restigouche Au showing; *SAR-Cu* indicate Saint-André-de-Restigouche Cu showing; *SF-Cu* indicate Saint-Fidèle Cu showing

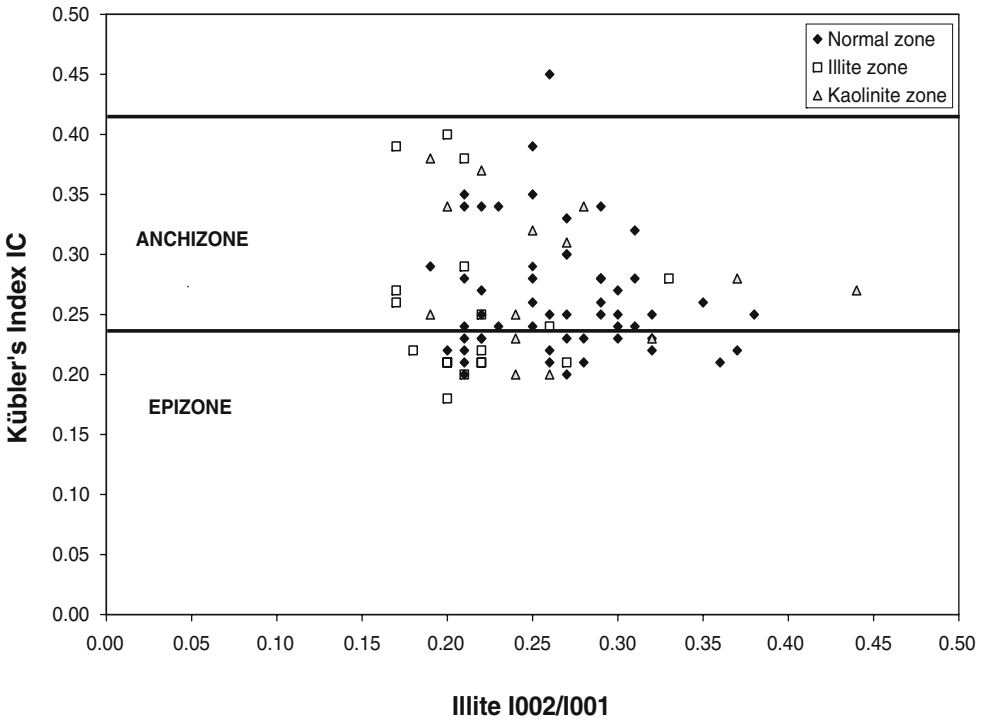

Fig. 7 Esquevin's diagram for illite from the normal, illite, and kaolinite zones

Table 1 Chemical analyses of samples from the main quartz vein, the silicified zone and the carbonatised zone at SAR-Au showing main vein, and from the protolith

Sample	SiO_2	Al_2O_3	CaO	MgO	Na_2O	K_2O	Fe_2O_3*	MnO	TiO_2	P_2O_5	Cr_2O_3	LOI	Total
Au-Sb-quartz vein													
04-MM-005-C7B	91.91	3.75	0.47	0.19	<0.01	0.25	1.24	<0.01	0.23	0.04	<0.01	1.85	99.94
CP-T09-1	90.29	2.39	0.68	0.42	<0.01	0.18	1.80	0.01	0.13	0.01	0.06	1.75	97.75
Silicified zone													
04-MM-005-C7C	87.65	4.01	2.19	0.93	<0.01	0.40	0.90	0.01	0.20	0.04	<0.01	3.75	100.10
04-MM-005-C7D	78.70	5.08	4.82	2.09	<0.01	0.47	1.41	0.03	0.27	0.05	<0.01	7.35	100.30
04-MM-005-C7E	61.96	7.65	9.30	3.77	<0.01	1.11	3.18	0.05	0.41	0.10	0.01	12.60	100.20
04-MM-005-C7F	82.31	5.42	3.59	1.39	<0.01	0.48	1.29	0.02	0.27	0.06	<0.01	5.55	100.40
04-MM-005-C7G	66.39	7.04	8.74	2.37	<0.01	0.87	3.03	0.04	0.35	0.08	<0.01	10.40	99.37
CP-T-18	77.46	6.86	4.25	1.86	<0.01	0.80	1.72	0.03	0.32	0.06	0.02	6.80	100.20
CP-T-07	84.63	4.42	2.73	0.92	<0.01	0.29	1.01	0.03	0.18	0.06	<0.01	5.08	99.38
CP-T11	76.17	7.66	2.03	1.19	<0.01	0.90	3.59	0.02	0.38	0.06	0.03	4.10	96.16
Carbonatized zone													
04-MM-005-C9A	14.08	3.81	41.81	1.27	0.04	0.86	1.75	0.04	0.19	0.04	<0.01	35.30	99.35
04-MM-005-C9B	17.14	5.40	36.79	2.99	0.04	1.41	2.52	0.05	0.27	0.05	<0.01	32.95	99.78
CP-T03	66.42	5.28	11.61	1.64	0.04	0.87	2.11	0.06	0.26	0.09	<0.01	11.30	99.73
CP-T05	18.15	4.46	37.87	2.97	0.07	0.98	2.00	0.04	0.21	0.04	<0.01	33.35	100.30
CP-T-25	21.36	1.85	40.49	0.96	0.03	0.30	1.17	0.04	0.08	0.02	<0.01	32.95	99.45
CP-T-15	74.07	4.68	7.13	2.42	<0.01	0.82	1.90	0.05	0.24	0.08	0.01	8.75	100.20
CP-T-08	82.73	1.38	8.38	0.22	<0.01	0.20	0.58	0.02	0.10	<0.01	<0.01	6.55	100.20
Protolith													
SA-03-001	20.41	5.02	35.49	2.88	0.56	1.14	2.54	0.05	0.25	0.04	<0.01	31.20	99.71
KM-03-015	9.09	2.17	46.07	1.30	0.20	0.38	0.99	0.02	0.11	0.01	<0.01	38.15	98.64
04-VG-010	34.12	8.37	23.80	3.78	0.99	1.64	4.18	0.09	0.46	0.08	0.02	22.70	100.40
04-VG-077	27.54	5.51	33.00	1.91	0.81	0.96	2.74	0.08	0.30	0.04	0.01	27.50	100.50
04-VG-055	21.36	6.43	35.16	1.88	0.41	1.17	2.92	0.08	0.32	0.05	<0.01	30.35	100.20
KM03-009	11.98	2.11	44.87	1.17	0.38	0.30	0.98	0.04	0.10	0.02	<0.01	36.85	98.92

All samples in wt. %
<, below detection limit
total Fe as Fe_2O_3

silicified and carbonatized country rocks, where Au grades reach up to 2 g/t and 0.962 g/t, respectively.

Element immobility and mobility can be identified using diagrams that show the concentration of one element in an altered vs a fresh sample (protolith). In these plots, immobile elements form a straight line that passes through the origin (Finlow-Bates and Stumpfl 1981; Grant 1986; Cail and Cline 2001) reflecting no mass change for these elements. A plot of SAR-Au showing TiO_2 vs Al_2O_3 produces a linear regression that passes through the origin with a r^2 of 0.97 (Fig. 8). The same covariation is also observed between V and Al (r^2=0.95) and between Zr and Al (r^2=0.94). These high r^2 values indicate immobile behavior for these elements in the altered sedimentary rocks of the SAR-Au showing, and they will be used to define the isocon (Fig. 9).

The composition of the protolith is estimated as the average of samples SA-03-001 and 04-VG-010 (Tables 1 and 2). The slope of the isocon represents the ratio of rock mass before alteration to rock mass after alteration (Grant 1986). The isocon is the line defined by Al_2O_3, TiO_2, Zr, and V (Fig. 9a–d). At the SAR-Au showing, the change in mass of the altered host rock varies from one sample to another, but elemental gains/losses are coherent between samples showing the same type of alteration. The isocon diagrams for samples from silicified alteration show enrichment in SiO_2, As, Sb, Au, and Hg and depletion in CaO, Mn, Fe, Cr, and Ag. Base metals exhibit erratic behavior, with minor enrichments and depletions (Fig. 9a,b; full diamonds). The silicification may be very intense, SiO_2 reaching up to 80 wt. % in some samples (Table 1; silicified zone). The altered rocks can be compared to replacement jasperoids typical of Carlin-type deposits and containing episodically silicified breccias, quartz vein stockworks, elevated As, Sb, Hg, Ba, and Tl, and locally anomalous Au and Ag (Nelson 1990; Table 2). Silicification is developed on 1–3 m on the eastern flank of the main vein No. 1, whereas carbonatization is developed for almost 2 m away from the selvages of the vein (Fig. 3). Samples from carbonatized alteration show enrichment in As, Sb, Au, and Hg (Fig. 9c,d). SiO_2 is enriched in some samples (Fig. 9d) but exhibits no significant change in concentration in other samples (Fig. 9c), whereas CaO exhibit minor erratic

Table 2 Metallic signature of the SAR-Au showing main vein and from the background

Samples	Au (ppb)	As (ppm)	Sb (ppm)	Hg (ppb)	Te (ppm)	Tl (ppm)	Ba (ppm)	Cu (ppm)	Zn (ppm)	Pb (ppm)	Ag (ppm)
Au-Sb-quartz vein											
CP-T04 (veinlet)	295	405	>100000	623	<0.1	0.3	2	6.3	2.6	<2	<0.2
CP-T09	>2000	7830	873	688			22	14.5	39.6	5	0.2
CP-T13-2_TR3	10660	5460	5210	113	0.5	<0.1	13	15.5	7.9	4	<0.2
04-MM-005-C7A	627	1400	>100000	635	0.3	0.2	4	13.1	3.3	<2	<0.2
04-MM-005-C7B	11380	4530	4590	285	0.5	<0.1	64	15.9	31.1	7	0.2
Silicified zone											
CP-T-07	744	990	162	100	0.2	<0.1	47	4.4	18.7	<2	0.2
CP-T11	>2000	>10000	74	519			95	23.3	55.2	5	0.2
92-CP-T-18	517	478	282	162	0.3	0.2	90	10.3	51.2	<2	0.4
92-CP-T-19	557	1210	148	128	0.3	0.2	106	12.5	42.5	<2	0.4
92-CP-T-20	519	895	1270	46	0.3	<0.1	56	6.2	16.9	<2	0.2
92-CP-T-22	18	1680	144	90	<0.1	0.2	116	7.6	27.3	<2	0.5
04-MM-005-C7C	897	831	169	121	0.1	<0.1	59	10.2	39.9	2	0.2
04-MM-005-C7D	216	307	148	173	0.1	<0.1	66	16.8	54.1	3	0.4
04-MM-005-C7E	155	397	198	201	0.2	0.2	124	14.1	52.7	5	0.4
04-MM-005-C7F	449	733	112	141	0.3	<0.1	62	14.7	35.8	3	0.3
04-MM-005-C7G	360	670	451	215	0.2	0.2	114	17.6	57.3	5	0.5
Carbonatized zone											
CP-T-08	28	122	503	49	0.3	<0.1	25	16.5	11.1	<2	0.3
CP-T-15	120	668	95	121	0.3	0.2	95	5.7	31.8	<2	0.3
92-CP-T-21	6	309	64	61	0.1	<0.1	66	4.9	11.6	<2	0.4
92-CP-T-24	962	1390	256	72	<0.1	0.1	68	7.5	23.2	<2	0.3
92-CP-T-26	<5	94	<50	164	0.2	0.3	185	17.6	45.8	7	0.6
92-CP-T-29	5	124	137	112	<0.1	0.2	138	14.4	33.4	2	0.6
04-MM-005-C9A	14	31	<50	58	<0.1	0.2	109	9.2	27.9	<2	0.5
04-MM-005-C9B	6	<30	<50	88	0.2	0.2	138	10.4	28.3	2	0.5
CP-T03	98	837	502	217			99	6	39.3	4	0.6
CP-T05	14	49	8	139			110	6.9	27.9	4	1.2
Protolith											
KM-03-015	10	5.2	<0.5	<5	<0.1	<0.1	56	7.5	16.5	<2	0.3
SA03-001	8	3.9	5	6	<0.1	0.2	145	12.2	30.7	3	0.6
04-VG-010	<5	12	<5	29			214	12	47.7	6	1.0
04-VG-077	<5	10	<5	20			128	9.4	34.4	3	1.2
04-VG-055	<5	5.0	<5	13			172	11.9	38.8	5	1.2
KM03-009	<5	4.0	<5	11			41	4.8	17.9	<2	1.0

enrichments and depletions (Fig. 9c,d, respectively). However, there is only a small variation in major oxides. This may indicate that the mineralizing fluids were in equilibrium with the host rocks. In addition, Au grades are highest in the most silicified rocks, highlighting a genetic link between the Au-Sb-As-quartz vein and the silicification of Au-bearing surrounding rocks (Tables 1 and 2).

In the silicified zone, Au is positively correlated to As content (Fig. 10a) but not to Sb content (Fig. 10b) suggesting that Au is associated with and possibly hosted by arsenopyrite and/or arsenian pyrite in altered limestones but not with stibnite. There is no correlation between Au and Hg, Cu or Zn. CaO and MgO depletions are consistent with carbonate dissolution during silica replacement. Samples from carbonatized alteration may show enrichment in CaO, in relation with late replacement of quartz in veinlets by calcite. Depletion in K in the silicified alteration is in agreement with the occurrence of kaolinite associated with gold mineralization at SAR, which results from the removal of K from detrital or diagenetic illite. W content is always below detection limit (10 ppm); Te and Tl contents are also often below detection limits or very low (Table 2).

Trace elements in pyrite and arsenopyrite

Trace-element contents in early stage pyrite and late stage pyrite overgrowth, and in arsenopyrite were analyzed by electron microprobe. The overgrowths of arsenian pyrite on early stage pyrite core are usually thinner than 1 μm (Fig. 11a,e), so analyses are often diluted by the surrounding

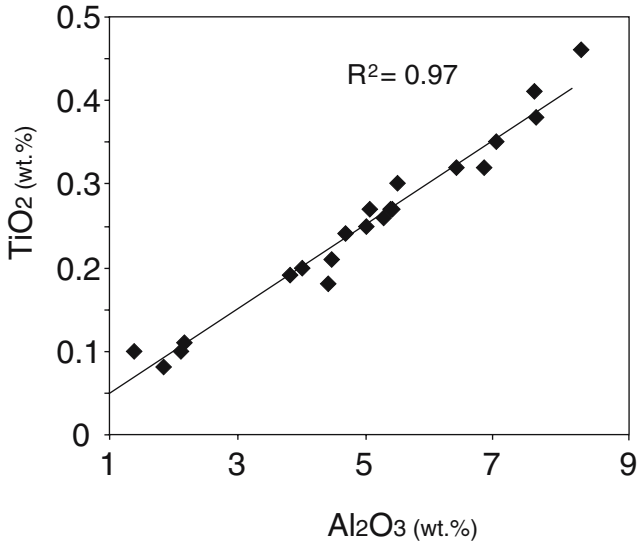

Fig. 8 TiO_2 vs Al_2O_3 diagram for samples from carbonated and silicified rocks, showing the correlation between both elements

material (early pyrite, carbonate, or quartz). The same dilution may affect core analyses when it is less than 5 μm thick. Early stage pyrite contains no detectable Au and usually nil to very low As: in most samples, As content in the core is below 1 wt. %, although in some As-rich samples, it may reach up to 3.9 wt. %, and low Sb (below 1,100 ppm), whereas late pyrite overgrowths are enriched in these elements: up to 15 wt. %, 2,280 ppm, and 2,850 ppm respectively for As, Au and Sb (Table 3, Fig. 11d,g). Most arsenopyrite contains up to 2,250 ppm Au and between 300 and 2,370 ppm Sb (Table 4; Fig. 11d,g). Sb in pyrite overgrowths and in arsenopyrite in quartz veins and veinlets support the hypothesis that the quartz-Au-Sb-As vein, silicification of the host rocks and Au-bearing arsenic-rich pyrite overgrowths were probably deposited by the same mineralizing fluid (Fig. 5). If the pyrite cores in silicified alteration are hydrothermal, their relatively low abundance in Au, As, and Sb indicate that they probably formed during an event that occurred before or earlier than the circulation of the fluid that has lead to the formation of the quartz-stibnite-Au vein.

Fluid inclusion analysis

Fluid inclusions were analyzed in quartz forming the quartz-carbonate-sulfides No. 1 vein. Quartz from silicified

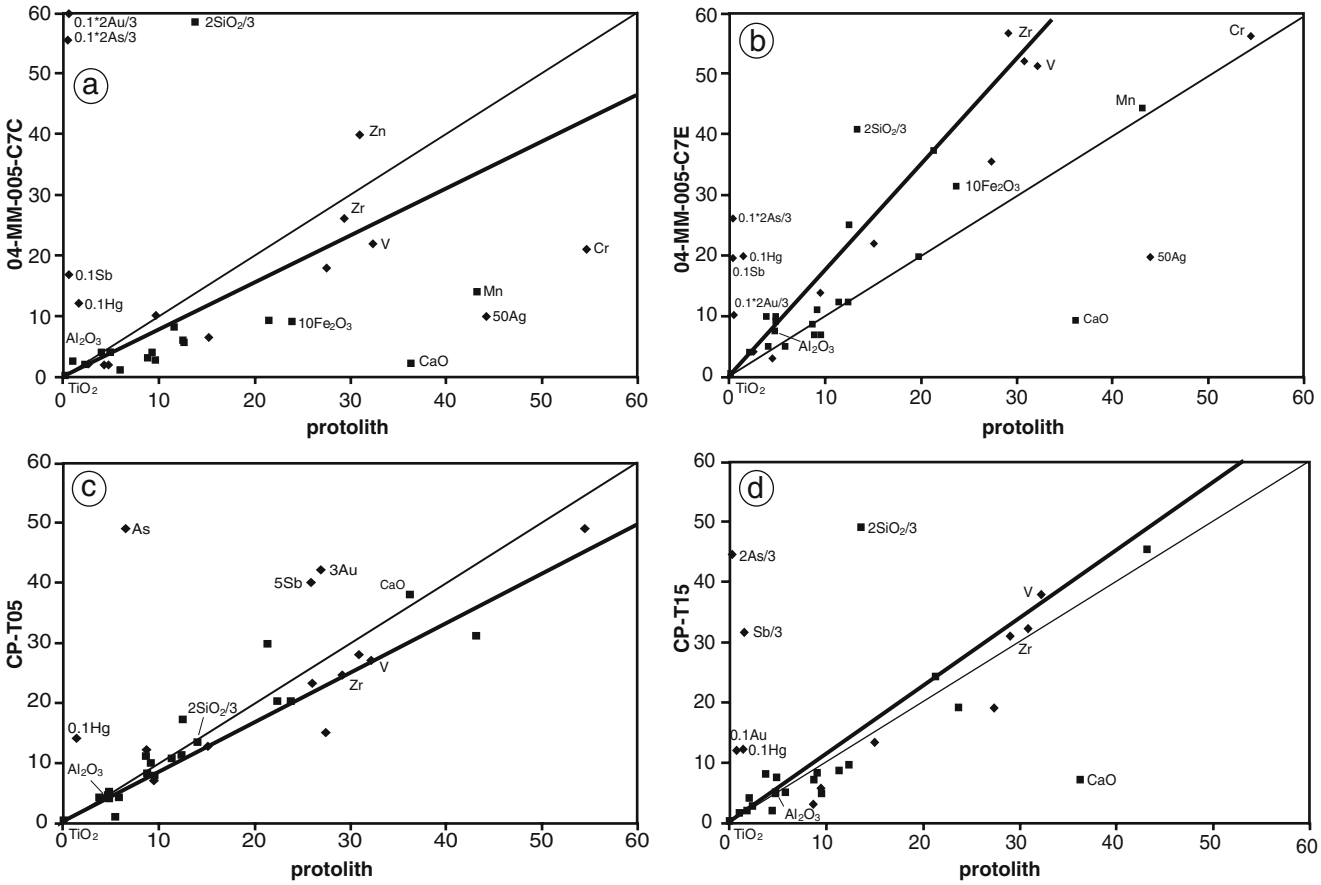

Fig. 9 Isocon diagrams for typical samples from the silicified (**a** and **b**) and from the carbonatized (**c** and **d**) zones. On each diagram, the *thick line* features the isocon drawn through immobile elements (Al, Ti, Ze, V), and the *thin line* is the line of constant mass. *Full diamonds* represent metals and metalloids, *full squares* for other elements. Data from Tables 1 and 2. Elements that display important gains/losses are labelled. The *protolith* corresponds to the mean values samples SA-03-001 and -04-VG-010 (Tables 1 and 2; see Fig. 6 for location)

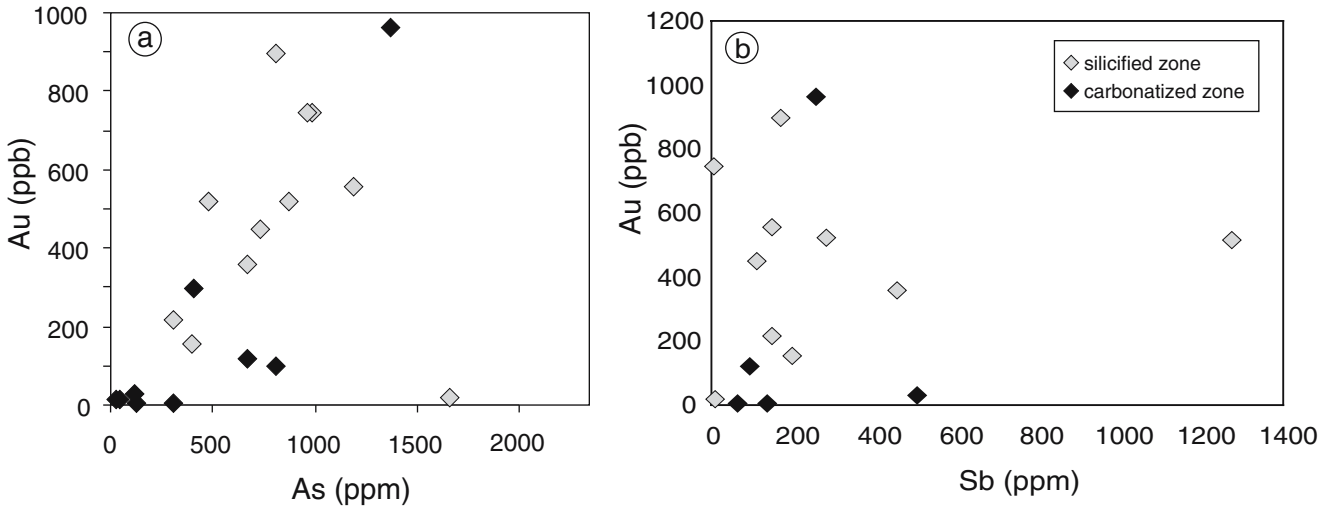

Fig. 10 **a** Au vs As contents and **b** Au vs Sb contents of samples from the SAR-Au showing

limestones contains only few fluid inclusions, which are too small for microthermometry. Fluid inclusions showing variable phase ratio at room temperature and a range of homogenization temperatures in the same fluid inclusions plane were not reported here as they may have suffered post-entrapment modifications.

Two types of pseudo-secondary fluid inclusions are distinguished in the quartz vein: (1) Fluid inclusions aligned with the arsenopyrite crystal faces, a few of them along the quartz–arsenopyrite crystals boundary. These inclusions trapped the fluid from which arsenopyrite deposited. All these pseudo-secondary aqueous fluid inclusions are small (generally between 5 and 8 μm) and contain two-phases with liquid/vapor ratio (L/V ratio) ranging from 10 to 20. They are interpreted to have trapped the mineralizing fluid from which arsenopyrite crystallised. Fluid inclusion analysis (FIA) show homogenization temperatures ranging from 135 to 246°C, with a median of 166°C (Fig. 12) and show salinities between 6.0 and 8.8 wt. % eq. NaCl with a median of 7.2 wt. % eq. NaCl. (2) Other pseudo-secondary fluid inclusion planes, not aligned with arsenopyrite in quartz vein. These fluid inclusions show no obvious relationship to the fluid circulation event that lead to deposition of arsenopyrite and could have trapped fluids that circulated after that event. They are thus considered separately from the previous type. They are also two-phases liquid-rich with L/V ratio between 10 and 20. The FIA show homogenization temperatures ranging from 117 to 277°C, and a median of 170°C. Th distribution is bimodal with peaks at 140–160°C and at 220–260°C. They show salinities between 3.6 and 8.0 wt. % eq. NaCl and a mode at 6.0–7.0 wt. % eq. NaCl (Fig. 12). Two fluid inclusions, one of each type, gave first melting temperatures of 21.0°C, indicating H_2O–NaCl composition for the fluid. Neither clathrate formation nor CO_2 melting were observed, indicating that, if present, CO_2 constitutes less than ~4 mol% of the mineralization fluid (Hedenquist and Henley 1985). Both types of fluid inclusions have similar characteristics but those not linked to the deposition of arsenopyrite exhibit higher homogenisation temperatures. In a temperature of homogenisation (Th) vs salinity diagram, both groups of pseudo-secondary fluid inclusions plot along an inverted "L" pattern (Fig. 13). Fluid inclusions with Th between 150 and 290°C and salinities ranging from 5.0 to 9.0 wt. % eq. NaCl show a range in temperature for constant salinity that is interpreted to document cooling of the fluid. The second trend of the pattern comprises fluid inclusions with Th ranging from 120 to 150°C and salinity from 3.6 to 7 wt. % eq. NaCl, which document dilution of the earlier high-temperature and high-salinity fluid.

Carbon and oxygen stable isotopes geochemistry

The oxygen isotope composition of quartz from the SAR quartz-stibnite-sulfides vein and carbon and oxygen isotope composition of silicified and mineralized calcilutites hosting the SAR vein are compared to the C–O isotope composition of unaltered whole-rock calcilutites (Fig. 14; Table 5). Whole-rock unaltered calcilutite has $\delta^{13}C_{VPDB}$ and $\delta^{18}O_{VSMOW}$ values ranging respectively from −0.1 to 1.1‰ and from 20.9 to 23.2‰ for calcite, and respectively from −0.2 to 1.2‰ and from 20.3 to 21.9‰ for dolomite. Silicified and mineralized calcilutites have $\delta^{13}C_{VPDB}$ and $\delta^{18}O_{VSMOW}$ values ranging respectively from −0.1 to 1.2‰ and from 21.3 to 23.6‰ for calcite, and from 0.2 to 1.4‰ and from 22.2 to 23.0‰ for dolomite. The C–O isotope composition of altered rocks is similar to that of unaltered

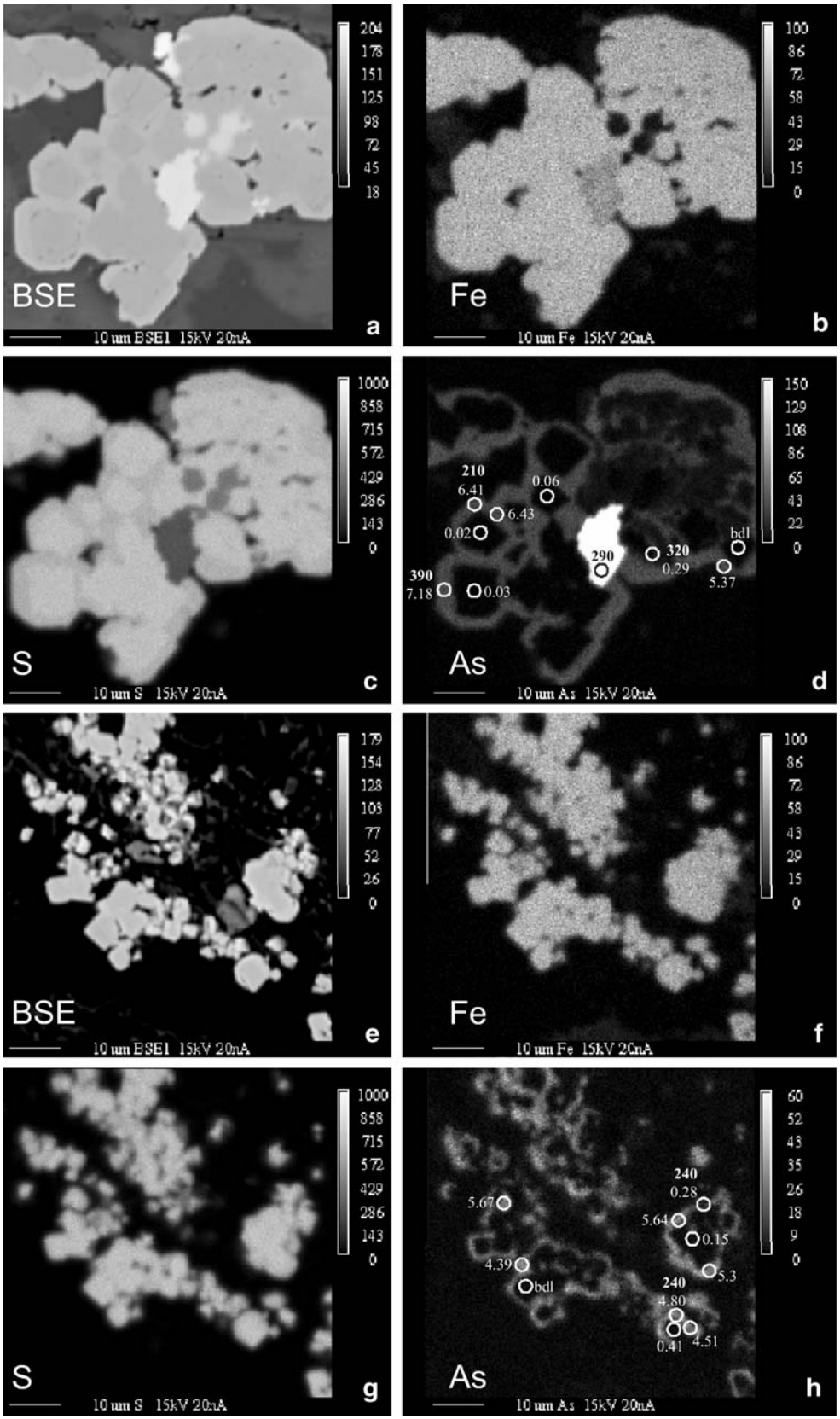

Fig. 11 Back-scattered electron images (BSE; **a**) and X-ray map for Fe (**b**), S (**c**), and As (**d**) in pyrite grains from sample CP-T18-2 (silicified zone; *top panel*). BSE (**e**) and X-ray map for Fe (**f**), S (**g**), and As (**h**) in pyrite grains from sample CP-T02-4 (carbonated zone; *bottom panel*). EPMA spots are also indicated with the respective Au (ppm, bold) and As (wt.%) contents. Bdl=below detection limit

Table 3 Electron microprobe analyses of pyrite cores and their arsenic-rich overgrowths form the SAR-Au showing main vein

	Sample	Fe (wt%)	S (wt%)	As (wt%)	Au (ppm)	Sb (ppm)	Total
Pre-ore stage pyrite	CP-T19	48.6	49.7	0.07	bdl	200	98.4
	CP-T18	47.2	47.6	0.41	bdl	230	
		47.7	51.4	0.15	bdl	140	99.3
		48.1	51.2	bdl	bdl	bdl	99.3
	CP-T02-4	48.0	50.6	0.02	bdl	bdl	98.6
		48.0	50.2	0.03	bdl	250	98.2
	CP-T05	46.7	50.4	0.58	bdl	180	97.7
		46.7	49.7	1.60	bdl	bdl	98.1
	CP-T27	47.0	50.7	0.05	bdl	140	97.7
		47.1	51.2	0.03	bdl	bdl	98.4
	CP-T11	47.1	49.9	2.65	bdl	bdl	99.6
		47.2	50.3	1.84	bdl	170	99.3
		46.4	51.4	0.56	bdl	410	98.4
	CP-T-13	46.2	49.5	1.10	bdl	590	
		48.1	51.3	0.03	bdl	bdl	99.4
		48.0	50.0	0.04	bdl	bdl	98.1
		47.8	50.7	bdl	bdl	bdl	98.5
		47.0	50.6	0.10	bdl	310	97.7
	CP-T03	47.7	50.3	0.04	bdl	230	98.0
	CP-T05	46.6	49.9	1.46	bdl	bdl	98.0
		46.6	50.8	0.48	bdl	550	97.9
Ore-stage pyrite	CP-T19	46.5	47.4	4.47	220	240	98.4
	CP-T18	45.2	45.1	4.80	240	bdl	
		47.3	50.3	0.28	240	bdl	97.9
	CP-T18	46.2	50.3	0.31	2280	420	97.0
		46.0	50.3	0.98	280	190	97.3
	CP-T02-4	46.0	46.9	6.42	210	830	99.0
		44.8	46.5	7.18	390	960	98.6
	CP-T05	43.4	45.4	6.67	250	460	
		43.1	44.7	7.29	220	1090	
	CP-T27	45.4	47.8	5.72	370	150	99.0
		44.7	46.7	6.44	270	160	97.9
	CP-T11	45.4	48.0	6.03	280	bdl	99.4
		44.8	43.8	6.48	270	bdl	
		43.7	42.4	15.09	350	220	101.2
	CP-T13	43.8	46.0	6.06	360	160	
		45.6	45.7	6.14	330	130	97.5
		45.5	45.7	8.91	240	680	100.2
		43.7	42.4	15.09	350	220	101.2
		46.8	48.8	3.72	360	240	99.3
		47.3	49.9	1.93	260	190	99.1
		45.3	45.8	5.63	260	250	
	CP-T05	46.5	41.0	0.37	280	280	
		46.6	40.6	5.22	1050	2480	
		43.0	43.6	5.42	220	500	

country rocks (Fig. 14). These values are typical of Ordovician marine carbonates ($\delta^{13}C = -2.5$ to 7‰ and $\delta^{18}O = 20.1$ to 29.4‰; Qing and Veizer 1994). The $\delta^{18}O_{VSMOW}$ values of quartz from the SAR vein and quartz veinlets in silicified calcilutite range from 21.7 to 23.7‰ (Table 5; Fig. 14). Calcite in late veinlets has $\delta^{13}C_{VPDB}$ and $\delta^{18}O_{VSMOW}$ values ranging from −4.3 to 1.4‰, and from 20.3 to 22.0‰, respectively. This range is similar to both unaltered and altered country rocks for oxygen but slighty lower values for carbon indicate a small contribution from a low $\delta^{13}C$ source (Table 5, Fig. 14). Late calcite veinlets yield $\delta^{18}O$ values similar to the unaltered host rocks but with $\delta^{13}C$ values slightly lower (to −4.3‰). As these veins formed late in the paragenetic sequence, it is most likely that they formed at temperatures lower than the main SAR quartz vein. Quartz vein fluid inclusions

Table 4 Electron microprobe analyses of arsenopyrite from the SAR-Au prospect main vein

	Sample	Fe (wt%)	S (wt%)	As (wt%)	Au (ppm)	Sb (ppm)	Total
Arsenopyrite	CP-T07	34.5	19.1	46.1	2378	414	100.0
		33.9	18.3	43.9	280	330	
		34.5	20.1	44.8	1270	760	99.5
		35.9	21.0	42.0	250	680	99.0
		35.9	20.9	43.8	bdl	2370	100.8
		35.5	20.2	44.0	620	2080	100.0
		35.7	21.7	43.0	bdl	390	100.4
		35.8	21.0	42.8	bdl	2040	99.9
		34.7	20.7	46.9	2520	620	
	CP-T02-4	35.9	20.8	44.2	bdl	1120	101.0
		32.3	20.2	44.4	bdl	660	
		35.5	20.8	44.1	290	1040	100.5
	CP-T11	35.5	19.9	45.9	1260	690	101.5
		35.4	20.2	45.8	bdl	450	101.4
		36.0	21.3	44.4	bdl	780	101.9
		36.1	20.4	45.1	300	730	101.7
		36.2	21.7	43.4	bdl	590	101.4
	CP-T13	36.7	21.7	42.0	370	410	100.5
		36.4	19.4	45.5	620	400	101.4
		35.5	19.2	46.0	370	450	100.8
		35.9	19.9	45.6	490	530	101.8
		35.6	19.6	45.6	bdl	340	100.8
		36.1	20.7	44.3	460	990	101.1
		35.9	20.0	44.8	500	1160	100.9
		36.1	20.7	43.5	350	1100	100.5
	CP-T18	35.9	20.7	45.0	bdl	1730	101.8
		35.1	20.8	44.7	bdl	990	100.7

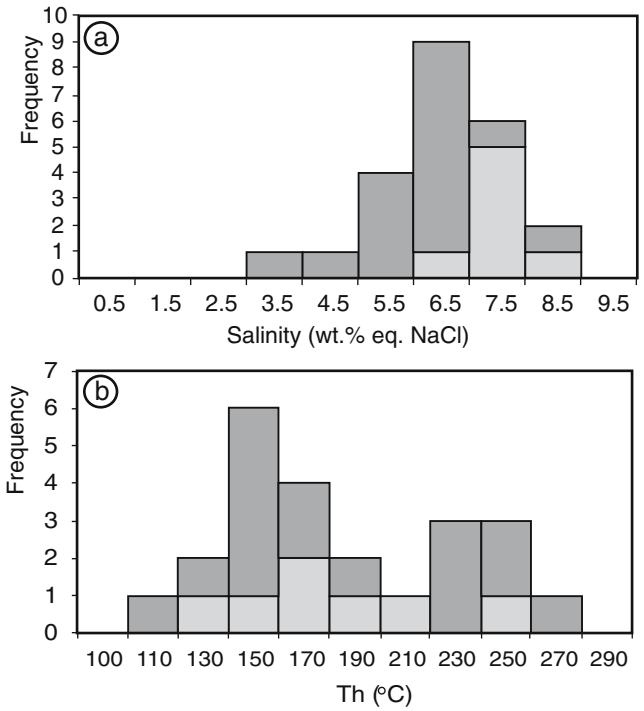

Fig. 12 Histograms of **a** salinity (wt.% eq. NaCl) and **b** homogenization temperatures (°C) in pseudo-secondary fluid inclusions in quartz from the main vein in SAR-Au showing, corresponding to the mineralizing fluid (*medium gray*) and other fluids (*dark gray*)

suggest that they formed at temperatures as low as 150–100°C.

Discussion

Tectono-stratigraphic setting during mineralization

A first constraint is represented by the maximal depth of formation of the SAR-Au showing. An estimation of 5–6 km is given by the thickness of Siluro–Devonian units covering the host limestones of the White Head Formation in southwestern Gaspé (Bourque et al. 1993). A second constraint is illustrated by the tectonic regime. The localization of the extensional Au-Sb-As quartz veins at SAR is structurally controlled by the last stage of the Acadian deformation (strike-slip faulting; Malo and Kirkwood 1995) because the veins are found along a releasing bend of the Restigouche fault. The open-space textures of the main vein and the orientation of the stockwork of veinlets parallel to this vein most likely indicate that it is an extension vein compatible with this dextral dilational jog. The depth is probably less than 5.5 km, because the tectonic uplift began during an earlier phase of the Acadian orogeny that preceded

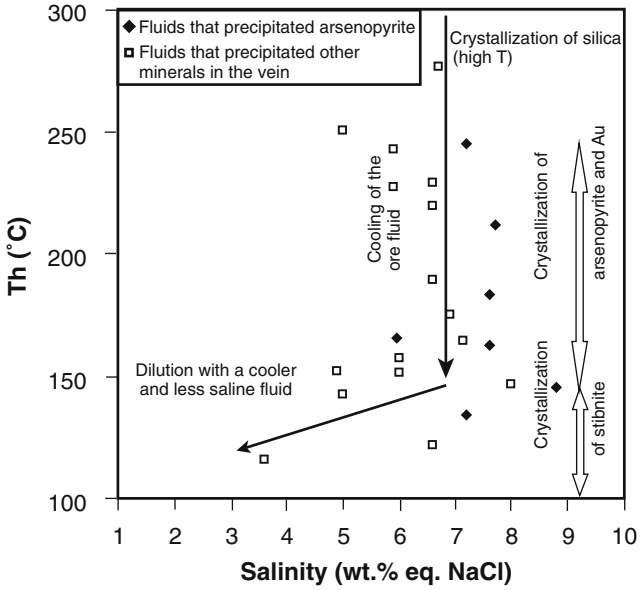

Fig. 13 Homogenization temperature (*Th*) vs salinity (wt.% eq. NaCl) diagram for pseudo-secondary fluid inclusions in quartz from the main vein at SAR-Au showing. (22 FIA and 6 samples)

strike-slip faulting (Malo 2001). This latter faulting is post Early Devonian in southwestern Gaspé because rocks of the Fortin Group along the Restigouche fault were affected by this strike-slip faulting (Fig. 6). Conglomerates from the Lagarde Formation, in southwestern Gaspé, contain fragments of the White Head Formation, indicating that the White Head limestones were in fact already in part emerged in the late Early Devonian.

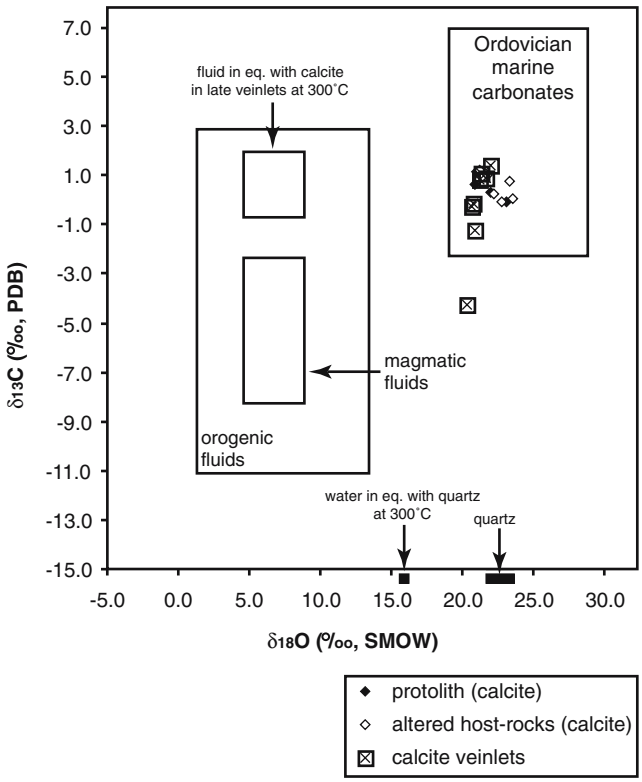

Fig. 14 $\delta^{18}O$ vs $\delta^{13}C$ diagram showing the distribution of SAR-Au showing rocks and veins. *Boxes* corresponding to Ordovician marine carbonates, orogenic fluids, and magmatic fluids are respectively from Qing and Veizer (1994), Hofstra and Cline (2000) and from Sheppard (1986) and Valley (1986)

Origin and evolution of clay mineral assemblages

The original terrigenous assemblage found in the White Head limestones was most likely formed of quartz, illite, chlorite, and feldspars with perhaps some illite/smectite mixed-layer minerals (Chagnon 1988). This original assemblage was subjected to burial metamorphism, which transformed illite/smectite to illite and increased the crystallinity degree of illite and chlorite as well as increased the reflectance of organic matter (Héroux and Chagnon 1986; Chagnon 1988). These two diagenetic indicators show that the sedimentary rocks in the SAR area have reached the anchimetamorphic–epimetamorphic levels. Even if they had been present at the time of sedimentation, kaolinite and smectite should have been recrystallized at such high temperatures (Héroux et al. 1979; Hoffman and Hower 1979; Kübler 1984). Because kaolinite and smectite are present in the insoluble residue of the White Head limestones, they should have formed after the maximum heating related to burial diagenesis, or to hydrothermal activity. Persistence of kaolinite and smectite also indicates that no significant heating occurred after their formation. The chlorite assemblage is very closely associated with skarns and was probably formed by reaction of the wall rock with magmatic fluids that produced the skarns. The smectite assemblage that generally surrounds the chlorite zone could have formed by alteration of chlorite by a later fluid, possibly after the the formation of the SAR-Au showing that is found within a kaolinite assemblage zone. The formation of smectite is most probably the last alteration episode that occurred in that system. The chronology of formation of kaolinite, kaolinite+smectite, and illite assemblages as well as fluid circulation patterns that formed the clay assemblages are difficult to establish. First, the chlorite is generally absent or in very small proportion in those assemblages, such that a relatively low pH fluid would be necessary to remove the Fe and Mg cations coming from the dissolution of chlorite. This low pH fluid would also have decarbonated the host rocks before silicification and precipitated kaolinite from a Si- and Al-rich fluid. K, Fe, and Mg were leached from the kaolinite zone by the fluid that replaced chlorite. Stability fields of these clay minerals and assemblages are controlled by the temperature and by the activities of such cations as Al, Si, Mg, Fe, K, and H. Activity diagrams in the system K_2O-MgO-Al_2O_3-SiO_2-H_2O have been produced by Aja et al. (1991). They show that the smectite is very temperature

Table 5 Carbon and oxygen isotopic composition of calcite and dolomite from the unaltered and from the silicified and mineralized host rocks, and from late calcite veinlets at SAR, and oxygen isotopic composition of quartz from the main quartz-stibnite-Au vein at SAR and quartz veinlets in the silicified calcilutites

Sample	calcite		dolomite		quartz vein
	$\delta^{13}C$(‰, PDB)	$\delta^{18}O$(‰, SMOW)	$\delta^{13}C$(‰, PDB)	$\delta^{18}O$(‰, SMOW)	$\delta^{18}O$(‰, SMOW)
Unaltered calcilutite (protolith)					
04-VG-055	0.3	22.0	−0.2	20.3	
KM-03-009	−0.1	23.2	0.1	21.9	
04-VG-010	0.6	20.9	0.8	21.5	
SA-03-001	1.1	21.0	1.2	20.6	
Mean	0.5±0.5	21.8±1.1	0.4±0.6	21.1±0.7	
Altered (silicified) and mineralized samples					
04-MM-005-C9B	1.0	21.7	1.4	22.2	
04-MM-005-Ch7E	0.7	23.3	1.3	23.5	
92-CP-T15	0.1	23.6	1.2	23.1	
91-CP-T11	0.2	22.2	0.2	22.9	21.7
91-CP-T07	−0.1	22.8	0.8	23.0	23.7
91-CP-T02	1.2	21.3			
91-CP-T18	0.9	21.4			
Mean	0.6±0.5	22.3±0.9	1.0±0.5	22.9±0.5	
Main SAR-vein					
91-CP-T13					23.1
91-CP-T04					22.6
Late calcite veinlets					
92-CP-T16	0.8	21.2			
92-CP-T25	−0.3	20.6			
91-CP-T05	1.1	21.4			
91-CP-T18	−0.2	20.8			
92-CP-T15	−4.3	20.3			
91-CP-T03	−1.3	20.8			
04-MM-005-C9B	0.9	21.7			
91-CP-T02	1.4	22.0			
Mean	−0.2±1.9	21.1±0.6			

dependent and has a very small stability field compared to that of kaolinite. For the illite assemblage, is it totally residual (sedimentary diagenetic) or a part of it could be epigenetic or could have precipitated after the chlorite dissolution. Figure 7 shows that the 002/001 X-ray diffraction peak ratios in the illite assemblage indicate that trioctahedral illite is more abundant than in the other assemblages. This is logical because the dissolution of the chlorite would have enriched the fluid in Fe and Mg. The fields are not completely distinct, because there is probably a mixture of the two kinds of illite, sedimentary and epigenetic.

Origin of the hydrothermal fluids

The trend of decreasing temperature from 300 to 150°C with a constant salinity (Fig. 13) likely represents cooling of the fluid as it percolates up through the fractured rocks. A temperature decrease will cause silica precipitation followed by arsenopyrite when the temperature reaches 300°C. Arsenopyrite crystallization ends when the temperature reaches 150°C, whereas silica will continue to precipitate at lower temperatures. The second trend with temperatures ranging from 150 to about 120°C records mixing between the cooled mineralizing fluid and another low temperature and low salinity fluid, most likely warm and exchanged meteoric water during the waning stage of the hydrothermal system.

The isotopic composition of water in equilibrium with the average SAR vein quartz $\delta^{18}O$ value (22.9‰) is estimated at the higher temperature end member of fluid inclusion data (300°C; Fig. 13), which yields a maximum $\delta^{18}O_{H2O}$ value of 16.0‰ using Clayton et al. (1972; Fig. 14). Quartz veinlets in silicified and mineralized calcilutite have $\delta^{18}O$ value similar to those from the SAR vein such that they formed from the same fluid. The oxygen isotope composition of water in equilibrium with the silicified and mineralized calcilutites (average $\delta^{18}O$ value, 22.3‰; Table 5), calculated for the same temperature (300°C) using the calcite-H_2O fractionation of O'Neil et al. (1969), yields $\delta^{18}O_{H2O}$ value of 16.7‰ (Fig. 14). The homoge-

neous oxygen isotope composition of SAR and veinlet quartz does not record the temperature gradient found in fluid inclusions (Fig. 13) suggesting that the bulk of the quartz most likely precipitated early, at the higher temperature end member. The similar $\delta^{18}O_{H2O}$ value for vein quartz and for the fluid in equilibrium with altered calcitlutite also suggests that the fluid composition was buffered by exchange with the carbonate wallrock at high temperature.

The oxygen isotope composition of water in equilibrium with late calcite veinlets was calculated at 4.5 and 9.0‰ respectively at 150 and 100°C using O'Neil et al. (1969). The C isotope composition of CO_2 in equilibrium with calcite from the veinlets, calculated using the calcite-CO_2 fractionation of O'Neil et al. (1969), ranges from −0.9 to 2.1‰. These values are compatible with extensive exchange of the fluids by the host rocks.

The C and O isotopic composition of calcilutites was not modified by exchange with the hydrothermal fluids that caused silicification. Exchange with magmatic fluids is expected to cause a strong decrease in $\delta^{18}O$ and $\delta^{13}C$ of the country rocks with a positive correlation in the host rocks (Valley 1986). Thus, the C and O isotopic composition of the mineralized calcilutites provides no evidence for infiltration of a pristine magmatic fluid, consistent with the high $\delta^{18}O$ fluid values (~16‰) calculated from hydrothermal quartz.

The most likely hypothesis is that the high $\delta^{18}O$ fluid (~16‰) had a temperature above 300°C and a salinity of about 7 wt. % NaCl. The oxygen isotopic composition, temperature, and salinity of this fluid suggest a water/rock exchange at high temperature, but lack of hydrous vein minerals prevent us from ascertaining more closely the origin of water between metamorphic and strongly exchanged sea or meteoric water. Cooling of the high-temperature fluid lead to quartz precipitation and sulfidation of host rocks that caused precipitation of gold in arsenian pyrite rims. In the waning stages of the hydrothermal system, lower temperature and lower salinity fluids, most likely exchanged sea or meteoric water, infiltrated and mixed with the cooled down high-temperature and high-salinity early fluid to precipitate stibnite in the SAR vein (Fig. 13).

The isotopic signature of the late calcite veinlets is consistent with dilution of the high-temperature and high-salinity hydrothermal fluid by sea or meteoric water. The host rocks contain a low abundance of organic matter (Héroux and Chagnon 1986) and thus oxidation of organic matter (CH_4) to CO_2 did not change the C isotopic signature of the paragenetically late calcite veinlets. The lower $\delta^{13}C$ values could be derived from surface water, which would be consistent with the retrograde solubility of carbonates and late paragenesis.

Timing of mineralization–alteration processes, igneous activity, and faulting

Spatial relationship of the Grand Pabos and Restigouche faults with the polymetallic base metal skarns, as well as with dike swarms (Fig. 1), suggests a genetic link between the faults, mineralization, and igneous activity. At the Reboul prospect (Fig. 1), a detailed study of crosscutting relationships between structural elements (folds, cleavages, veins, shear fractures), the three types of mineralization locally present (early Cu-Zn-Ag stratabound skarn, Cu-Zn-Pb-Ag-[Au] and Ag-Cu-Zn-Pb-[Au-Sb] northeast- and northwest-trending veins, and late Ag-Au-Zn-Pb breccia veins), and the alteration indicates that the mineralization–alteration processes occurred during the development of the Grand Pabos fault (Malo et al. 2000). Fluid inclusion data from the early Cu-Zn-Ag mineralization at Reboul, as well as from the Cu skarn at the Mid-Patapédia prospect (Fig. 1; mineral occurrence 9), indicate that a high-temperature (Reboul, 450–460°C) and high-salinity (Reboul, 35–37 wt. % eq. NaCl) magmatic fluid was involved in the genesis of both skarns (Williams-Jones 1982; Williams-Jones and Ferreira 1989; Malo et al. 2000). The zoned halos of argillaceous alteration centered on Cu skarns (Fig. 6) also support a genetic link with igneous rocks at depth. At the Reboul prospect, the two later types of mineralization and alteration facies were accompanied by a decrease in temperatures, as indicated by fluid inclusions (350–200°C), and an enrichment in precious metal (Au and Ag; Malo et al. 2000). Hydrothermal fluids were also less saline (1–9 wt. % eq. NaCl: Malo et al. 2000). At SAR-Au, the high-temperature and high-salinity magmatic fluid associated with the early development of skarns is not recognized, but hydrothermal fluids have characteristics very close to those of the two late mineralizations at the Reboul prospect (low temperature/low salinity). Limestones of the White Head Formation were already folded and cleaved at the time of alteration and emplacement of mineralized veins at the Reboul prospect, but also at SAR-Au (Fig. 3). At SAR-Au, as well as at the Reboul prospect, halos of argillic alteration are cut by the Restigouche and Grand Pabos faults, respectively, suggesting that regional alteration predate Acadian strike-slip faulting (Malo et al. 2000). However, at the Mid-Patapedia prospect (Fig. 1), hydrothermal alteration halos are found on both sides of the Restigouche fault (Duba and Williams-Jones 1983) indicating that hydrothermal fluids continued to percolate along the fault after the main Acadian dextral strike-slip motion. The Acadian faults were reactivated after the Carboniferous because the Grand Pabos fault offsets rocks of the Carboniferous basin north of Chandler (Fig. 1; see also Jutras et al. 2003), and younger fluid circulation associated with post-Acadian motion along the fault is not ruled out.

Table 6 Comparison of the main characteristics of orogenic epizonal Au–Sb deposits, distal-disseminated Au deposits and Carlin-type Au deposits

	Orogenic epizonal Au–Sb	Distal-disseminated Au deposits	Carlin-type Au deposits
Tectonic setting	Continental margin; compressional to transpressional regim; veins typically in metamorphic rocks on seaward side of continental arc[c] Epizonal Au–Sb deposits are often hosted in accretionary prism, accreted arc, turbidites and metagreywacke[a]	Within magmatic arc±extension[f]	Back-arc extension and thinning of continental crust[c] in diffuse magmatic arc, onset of extension[f]
Structural style	Ductile to brittle-ductile, reverse, strike-slip faults or oblique-slip; anticlinal domes[g]		Long-lived, crustal fracture zones[f]
Associated igneous rocks	Commonly felsic to lamprophyre dikes or continental margin batholiths[d]	Calc-alkaline, subduction related[f]	Broad spatial correlation with calc-alkaline subduction-related magmatism[f]
Nature and form of ore bodies	Veins, breccias, disseminated style[g]	Discordant and strata bound[f]	Discordant and strata bound[f]
Host rocks	Mafic and ultramafic volcanic rocks, intrusive rocks, BIF-chert, graywacke[g]	Calcareous sedimentary rocks of diverse facies and igneous intrusions[f]	Calcareous sedimentary rocks of diverse facies±igneous rocks[f]
Ore minerals, residence of gold and metallic minerals	Native gold, pyrite±arsenopyrite, stibnite, electrum, scheelite, galena, chalcopyrite, pyrrhotite, sphalerite[a]	Chalcopyrite, tetrahedrite, sphalerite, galena, pyrite, pyrrhotite, arsenopyrite[f] Au: free, inclusions in solid solutions in chalcopyrite, tetrahedrite, pyrite and arsenopyrite	Ionic substitution and submicron-sized grains in arsenian-pyrite[h] forming overgrowths on pre-ore As-free or poor and Au-free pyrite
Metal association	Au, Ag, ±As, Sb, Te, W, Bi[g]	Various base metals, Mn, As, Sb, Te, Ag, Au±Ba[f]	Au, As, Sb, Tl, Hg±W, Te, Se, Ba[f]
Temperature of formation	150–300°C[c]	200–400°C[f]	200–300°C[c], 150–250[j]C[f]
Depth of formation	0–6 km[c]	Variable, 0.5 to 8 km[f]	2–3 km[c]; intermediate, mainly >2 km[f]
Ore fluid composition	Low salinity, aqueous-carbonic±H_2S[g]; 3–10 eq. wt.% NaCl; =5 mol.% CO_2; traces of CH_4 and N_2[c]	Variable salinity, variable CO_2 and H_2S, ± boiling[f]	≤7 eq. wt% NaCl[c] low salinity, 2–4 mole % CO_2, 0.01 mole % H_2S[f]
Au/Ag	1–10[1], avg ~5[g]	Low, variable, up to 3[f]	0.1–10[c], high, >3 to 20[f]
Alteration types	Carbonation, sericitization, sulfidation; skarn-like assemblages in higher temperature deposits[c] Muscovite, Ca-Fe-Mg carbonates, chlorite, albite, pyrite, tourmaline[g]	Potassic, phyllic, argillic, decarbonation, silic[f]	Intense silicification; some kaolinization[cf] Decarbonation, argillic alteration, silification, sulfidation
Heat sources	Asthenosphere, crust[g]; asthenosphere upwelling to midcrustal granitoids		In Nevada, deep crustal melting and prograde metamorphism promoted by the removal of the Farallon slab[b]
Fluid sources	H_2O: meteoric and/or metamorphic as a fluid source	H_2O: magmatic and meteoric[f]; CO_2: magmatic, decarbonation of limestone[f], H_2S: magmatic, sedimentary rocks[f], prophyry intrusions[e]	H_2O: meteoric and/or metamorphic; CO_2: metamorphic-carbonate rocks; H_2S: sedimentary-metasedimentary rocks[f]

[a] Ashley and Craw (2004) and references therein; [b] Cline (2005); [c] Groves et al. (1998); [d] Groves et al. (2003); [e] Hofstra (1997); [f] Hofstra and Cline (2000); [g] Kerrich et al. (2000); [h] Muntean et al. (2004); [i] Schroeter and Poulsen (1996); [j] Theodore (1998)

Comparison with Carlin-type and other types of gold deposits

Table 6 synthetizes the characteristics of three types of gold deposits: (1) orogenic epizonal Au-Sb veins, (2) distal-disseminated Au-deposits, and (3) Carlin-type gold deposits. The association with strike-slip fault and the metallic signature of the SAR-Au showing (Au-As-Sb) are characteristics common to epizonal orogenic Au–Sb veins (Groves et al. 1998). However, the nature of the host rocks, of the alteration, and of the mineralization fluid (Table 6) are not typical of epizonal Au–Sb deposits. The SAR-Au showing shares strong analogies with sedimentary rock-hosted, disseminated gold deposits. These deposits have been separated into two specific types: Carlin-type and distal-disseminated Au–Ag deposits (Johnston and Ressel 2004). Although both types of deposits share many physical and geochemical characteristics, the distal-disseminated deposits are distinguished from Carlin-type deposits, based on more definitive chemical, spatial, and/or temporal links with porphyry-related deposits (Johnston and Ressel 2004). In contrast to distal-disseminated deposits, Carlin-type deposits generally form at lower temperatures, are commonly not spatially associated with metamorphic aureoles of coeval intrusive stocks, lack Ag and base metal association, and have fluid isotope compositions suggesting evolved meteoric fluids in metasedimentary rocks as sources for ore-forming components (Johnston and Ressel 2004). Although some authors clearly distinguish distal-disseminated gold deposits from Carlin-type (Cunningham et al. 2004), others wonder whether the variability in isotopic and metal signatures across the sedimentary rock-hosted Au deposit spectrum could be related to the distance from source magmas and degree of mixing and dilution of magmatic fluid by meteoric water rather than distinguishing between mutually exclusive magmatic and amagmatic contributions (Johnston and Ressel 2004; Sillitoe 2004). The chemical distinction between both types of deposits is not obvious, as Te, W, Ag, and relatively minor quantities of Zn, Pb and Cu occur in several classic Carlin-type deposits (Hofstra and Cline 2000). However, base metals are usually downplayed or ascribe to pre-Au diagenetic or hydrothermal activity (Sillitoe 2004). On the other hand, base metals are not reported to be anomalous in certain deposits peripheral to several intrusion-centered districts (Babcock et al. 1995). Furthermore, classic Carlin-type deposits typically lack isotope evidence for magmatic input (Hofstra and Cline 2000; Hu et al. 2002), although recent results from Deep Star, Screamer, and Getchell are consistent with contributions of magmatic volatiles and/or S (Cline et al. 2003; Heitt et al. 2003; Kesler et al. 2003). The role played by magmatism in the formation of Carlin-type deposits in Nevada is still debated (Muntean et al. 2004).

Although the spatial association of the SAR-Au showing with Cu-skarn and porphyry mineralization is characteristic of distal-disseminated Au deposits, the lack of definitive evidence for a magmatic-derived hydrothermal fluid and the absence of base metals and silver enrichment at SAR-Au showing are inconsistent with this type of deposit.

The principal characteristics of Carlin-type gold deposits from Nevada are summarized by Schroeter and Poulsen (1996), Hofstra (1997), Poulsen (1999a, b), Groves et al. (1998), Hofstra and Cline (2000), and Cline (2005) in Table 7. Carlin-type gold deposits are described as sedimentary rock-hosted disseminated gold deposits, associated with jasperoid replacements of limestones. It is notable to mention that most of the characteristics are found at the regional scale, Gaspé Peninsula, and northern New Brunswick (Fig. 1), at the district scale, southern Gaspé (Fig. 1), and at the occurrence scale, the SAR-Au showing. The most striking features found in the SAR-Au showing that are compatible with Carlin-type deposits are: (1) the calcareous nature of the host rocks; (2) the Au-As-Sb-Hg metallic signature with absence of base metals and Ag (Hofstra and Cline 2000); (3) the association with a crustal scale fault zone; (4) the hydrothermal alteration characterized by silicification, calcite and quartz veinlets at the margin of the Au-bearing zones and the occurrence of kaolinite in large halos of argillic alteration; (5) numerous felsic dikes; (6) the occurrence of Au in As-rich pyrite

Table 7 Principal characteristics of Carlin-type deposits from Nevada (Poulsen 1999b) and their presence or absence at SAR-Au showing

Regional scale		District scale		Occurrence scale	
Carbonate assemblages	√	Siliciclastic carbonates	√	Microscopic gold	√
Facies boundary	√	Thrusts (reverse faults)	√	Silicification	√
Major lineaments	√	Anticlines/horsts	√	As-Sb-Au-Hg	√
Allochthons	X	Strike-slip/normal faults	√	Breccias	√
Unconformities	√	Intrusions/stocks	√	Steep faults	√
Mineral belts	√	Jasperoids	√	Impure carbonate host	√
Magmatic belt	√	Other gold occurrences	√	Siliciclastic/volcanic caps	√
Core complexes	X			Dikes	√

forming overgrowths on pre-ore As-free pyrite, and in arsenopyrite; (7) hydrothermal fluids mainly derived from meteoric water exchanged with host rocks at high temperature (>200°). In addition, Peters et al. (1997), Emsbo et al. (2003), and Nutt and Hofstra (2003) describe breccias formed by jasperoid and limestone clasts cemented by drusy quartz±stibnite, similar to those observed at SAR-Au showing. These breccias are interpreted by Nutt and Hofstra (2003) to be pre- or syn-ore, because the oxygen isotope compositions of drusy quartz are similar to those of gold-bearing jasperoid. In addition, at Meikle, stibnite veins cut across breccia cavities filled by ore. The silicified limestones at SAR-Au showing are comparable with the jasperoids replacement of limestones commonly found in Carlin-type gold deposits. However, the size of the SAR-Au showing is significantly smaller than in typical Carlin-type deposits in Nevada. At the regional scale (Table 7), there are differences between tectonic setting of the Nevada region and southern Gaspé Peninsula. Carlin-type deposits in Nevada are mainly hosted by Paleozoic platform rocks overthrust by offshore volcanic and siliciclastic Paleozoic rocks. During the mid-Tertiary, the region was subsequently affected by regional extension and calc-alkaline subduction-related magmatism (Hofstra and Cline 2000). Carlin-type deposits were mainly formed during this latter time interval (Hofstra et al. 1999). Temporal and spatial links with mid-Tertiary magmatic belts suggest a genetic relationship with Carlin-type gold deposits (Hofstra and Cline 2000). In the Gaspé Peninsula, the SAR-Au showing is hosted by deep-water carbonate rocks deposited in a successor basin. This basin was affected by Late Silurian normal faulting during the Salinic disturbance (Malo 2001) and subsequently folded and faulted (high angle and strike slip) during the Devonian Acadian orogeny (Malo and Kirkwood 1995). The Acadian tectonic regime in southern Gaspé is dominated by strike-slip tectonics (Malo and Kirkwood 1995), and volcanic rocks are of within-plate affinity (Bourque et al. 2001). The tectonic setting of the Carlin-type deposits in Nevada is more complex, involving more than one major orogenic event, Paleozoic and Mesozoic compressive deformation followed by Tertiary extension (Hofstra and Cline 2000). The type of magmatic regime is also very different between subduction-related magmatism in Nevada and within-plate magmatism in the Gaspé Peninsula.

Exploration guides

Although the SAR-Au showing is small, the analogies with Carlin-type mineralizations encourages exploration for such a deposit type in the area and elsewhere in the Appalachians as already proposed in Newfoundland by Squires (2004).

Malo et al. (1998) proposed that the southwestern Gaspé area could represent an intrusion-related hydrothermal center with proximal Cu-skarn mineralization and distal Carlin-type Au-As-Sb±Hg mineralization. This magmatism likely raised temperature and could have induced convection of the mineralizing fluid at depth. The distribution of magmatic rocks in the region may serve as a guide, as magmatism was probably the source of the mineralizing fluid or at least of heat necessary to convect the ore-fluid.

The quartz-stibnite-Au mineralization at SAR-Au showing is controlled by the Grand Pabos-Restigouche fault system. Structural intersections between secondary faults/shear fractures and the main Grand Pabos-Restigouche faults are prime targets in exploration for new deposits. In addition, zoned halos of clay mineral assemblages are very useful mineral exploration tools as all Au showings, as well as Cu-skarns, in the area (Fig. 6) are within clay minerals halos. A 1-km side square sampling grid seams suitable for the exploration for such halos. However, precise drawing of the halos would necessitate a sampling grid with smaller cells (about 0.5 km side square cells).

A low coast approach to support an exploration program could be a regional stream sediment survey analyzing among others As and Au with very low detection limits.

Conclusion

This study highlights the analogy of the geological setting of the SAR area with that of regions hosting Carlin-type mineralization. The collective geological characteristics of the SAR-Au showing indicate that it shares many characteristics with the Carlin-type gold deposits of Nevada. The most diagnostic feature is the occurrence of Au in arsenian pyrite overgrowths on early and arsenic-free pyrite. In addition, the metallic signature and the alteration style are similar to those in Carlin-type mineralizations from Nevada. The mechanisms that lead to the formation of Carlin-type gold deposits are still under debate. However, the origin of the mineralizing fluid that lead to the formation of SAR-Au showing is not in contradiction with Carlin-type gold deposits.

This study reveals new types of mineralization in the Canadian Appalachians and highlights new guides for the prospecting of other occurrences, such as clay mineral halos and structural features.

Acknowledgements This study was supported by the Québec research network Diversification de l'exploration minérale (DIVEX), and we would like to acknowledge Valorisation Recherche Québec for a grant to DIVEX. We also want to thank Marc Choquette, Jean Frenette, and Martin Plante from Université Laval, respectively for SEM and electron-probe analysis, for DRX analyses, and for stable isotopes analysis of quartz. We thank also Marc Luzincourt from the GSC-Delta Lab for isotopic analyses of carbonates. We are grateful to Émilie Tremblay-Paquet and Stéphanie Roy for their assistance in the field work. We are also grateful to G. Chi, D. Lentz, P. Pilote, and L.D.

Meinert for their constructive reviews and comments that improved the quality of the manuscript. M. Malo and G. Beaudoin acknowledge long-term funding by Discovery grants from the National Science and Engineering Research Council of Canada.

References

Aja SU, Rosenberg PE, Kittrick JA (1991) Illite equilibria in solution. II. Phase relationships in system K_2O-MgO-Al_2O_3-SiO_2-H_2O. Geochim Cosmochim Acta 55:1365–1374

Al-Aasm I, Taylor BE, South B (1990) Stable isotope analysis of multiple carbonate samples using selective acid extraction. Chem Geol 80:119–125

Ashley PM, Craw D (2004) Structural controls on hydrothermal alteration and gold-antimony mineralization in the Hillgrove area, NSW, Australia. Miner Depos 39:223–239

Babcock RC, Ballantyne GH, Phillips CH (1995) Summary of the geology of the Bingham district, Utah. Ariz Geol Soc Dig 20:316–335

Berger BR, Bagby WC (1991) The geology and origin of Carlin-type gold deposits. In: Foster RP (ed) Gold metallogney and exploration. Blackie and Son, Glasgow, Scotland, pp 210–248

Bourque PA, Gosselin C, Kirkwood D, Malo M, St-Julien P (1993) Le Silurien du segment appalachien Gaspésie-Matapédia-Témiscouata: stratigraphie, géologie structurale et paléogéographie. Ministère de l'Énergie et des Ressources, MB 93–25, p 115

Bourque PA, Malo M, Kirkwood D (2001) Stratigraphy, tectono-sedimentary and paleogeography of the Post-Taconian-Pre-Carboniferous Gaspé Belt: an overview. Bull Can Pet Geol 49: 186–201

Cail TL, Cline JS (2001) Alteration associated with gold deposition at the Getchell Carlin-type gold deposit, North Central Nevada. Econ Geol 96:1343–1359

Chagnon A (1984) Indice aigu de l'illite et minéralogie des argiles de la région de St-André-de-Restigouche. Ministère de l'Énergie et des ressources du Québec, GM 40812, p 19

Chagnon A (1988) Géologie des argiles, diagenèse et altération hydrothermale, dans l'anticlinorium d'Aroostook-Percé, Québec (Canada). D.Sc. thesis, Université de Neuchâtel, Switzerland, p 367

Chagnon A, Desjardins M (1991) Détermination de la composition de la chlorite par diffraction et microanalyse aux rayons X. Can Mineral 29:245–254

Chagnon A, Malo M (1991) Hydrothermal clay mineral assemblages related to mineralized skarns along the Grand Pabos-Matapédia fault, southern Gaspé Peninsula. GAC-MAC annual meeting, Program with abstracts, p 21

Clayton RN, Mayeda TK (1963) The use of bromine pentafluoride in the extraction of oxygen from oxides and silicates for isotopic analyses. Geochim Cosmochim Acta 27:43–52

Clayton RN, O'Neil JR, Mayeda TK (1972) Oxygen isotope exchange between quartz and water. J Geophys Res 77:3057–3067

Cline JS (2005) The genesis of Carlin-type gold deposits—current models and future research. GAC Newfoundland section, 2005 technical meeting, St. John's, Program and abstracts, pp 11–13 (February 21–22)

Cline JS, Shields D, Riciputi L, Fayek M, Copp TL, Muntean J, Hofstra AH (2003) Trace element and isotope micro-analyses support for deep ore fluid source at the Getchell Carlin-type gold deposit, northern Nevada. Proc Geol Soc Am Abstr Prog 35 (6):358

Cunningham CG, Austin GW, Naeser CW, Rye RO, Ballantyne GH, Stamm RG, Barker CE (2004) Formation of a paleothermal anomaly and disseminated gold deposits associated with the Bingham Canyon porphyry Cu-Au-Mo system, Utah. Econ Geol 99:789–806

Daigle R (1990) Levés géophysiques de Saint-André-de-Restigouche. Ministère de l'Energie et des Ressources du Québec, GM 49415, p 10

Dessureault M (1990) Travaux de mise en valeur de la propriété Beaulieu-Vallée-Roy. Ministère de l'Énergie et des Ressources du Québec, GM 50165, p 208

Doyon M, Berger J (1997) Distribution et contrôles structuraux des roches magmatiques siluro-dévoniennes de la Gaspésie. Ministère des Ressources naturelles du Québec, ET 97-01, p 31

Duba D, Williams-Jones AE (1983) Studies of burial metamorphism in the post-Taconic stages of the Appalachian orogen, southwestern Gaspé. Can J Earth Sci 20:1152–1158

Emsbo P, Hofstra AH, Lauha EA, Griffin GL, Hutchinson RW (2003) Origin of high-grade gold ore, source of ore fluid components, and genesis of the Meikle and neighboring Carlin-type deposits, Northern Carlin Trend, Nevada. Econ Geol 98:1069–1105

Esquevin J (1969) Influence de la composition chimique des illites sur leurs cristallinités. Centre de Recherche de Pau, Société Nationale des Pétroles d'Aquitaine Bulletin 3:147–154

Finlow-Bates T, Stumpfl EF (1981) The behaviour of so-called immobile elements in hydrothermally altered rocks associated with volcanogenic submarine-exhalative ore deposits. Miner Depos 16:319–328

Gauthier M, Chartrand F, Trottier J (1994) Metallogenic epochs and metallogenic provinces of the Estrie-Beauce region, southern Quebec Appalachians. Econ Geol 89:1322–1360

Goldstein RH, Reynolds TJ (1994) Systematics of fluid inclusions in diagenetic minerals. Society of Sedimentary Geology Short Course 31, SEPM, Tulsa, OK, p 199

Grant JA (1986) The isocon diagram: a simple solution to Gresens' equation for metasomatic alteration. Econ Geol 81: 1976–1982

Groves DI, Goldfarb RJ, Gebre-Mariam M, Hagemann SG, Robert F (1998) Orogenic gold deposits: a proposed classification in the context of their crustal distribution and relationship to other gold deposit types. Ore Geol Rev 13:7–27

Groves DI, Goldfarb RJ, Robert F, Hart CJR (2003) Gold deposits in metamorphic belts: overview and current understanding, outstanding problems, future research, and exploration significance. Econ Geol 98:1–29

Hedenquist JW, Henley RW (1985) The importance of CO_2 on freezing point measurements of fluid inclusions: evidence from active geothermal systems and implications for epithermal ore deposition. Econ Geol 80:1379–1399

Heitt DG, Dunbar WW, Thompson TB, Jackson RG (2003) Geology and geochemistry of the Deep Star gold deposit, Carlin trend, Nevada. Econ Geol 98:1107–1135

Héroux Y, Chagnon A (1986) Relation entre l'hydrothermalisme, les aires d'altération, les indices minéralisés et la diagenèse des matières organiques des groupes d'Honorat, de Matapédia et de Fortin dans les régions de Saint-André-de-Restigouche et de Carleton, Gaspésie. Ministère de l'Énergie et des Ressources du Québec, MB 86-61, p 52

Héroux Y, Chagnon A, Bertrand R (1979) Compilation and correlation of the major thermal indicators. Am Assoc Pet Geol Bull 63:2128–2144

Hoffman J, Hower J (1979) Clay mineral assemblages as low grade metamorphic geothermometers : application to the thrust faulted disturbed Belt of Montana, U.S.A. In : Scholle PA, Schluger PR (eds) Aspects of diagenesis. Society of Economic Paleontologists and Mineralogists, Special Publication 26:55–80

Hofstra AH (1997) Isotopic composition of sulfur in Carlin-type gold deposits: implications for genetic models. In: Vikre P, Thompson

TB, Bettles K, Christensen O, Parratt R (eds) Carlin-type gold deposits field conference. SEG Guidebook series 28:119–129
Hofstra AH, Cline JS (2000) Characteristics and models for Carlin-type gold deposits. SEG Rev 13:163–220
Hofstra AH, Snee LW, Rye RO, Folger HW, Phinisey JD, Loranger RJ, Dahl AR, Naeser CW, Stein HJ, Lewchuk M (1999) Age constraints on Jerrit Canyon and other Carlin-type gold deposits in the Western United States-relationship to mid-tertiary extension and magmatism. Econ Geol 94:769–802
Hu RZ, Su WC, Bi XW, Tu GZ, Hofstra AH (2002) Geology and geochemistry of Carlin-type deposits in China. Miner Depos 37:378–392
Johnston MK, Ressel MW (2004) Carlin-type and distal-disseminated Au-Ag deposits: related distal expressions of Eocene intrusive centers in North-Central Nevada. In: Muntean JL, Cline J, Johnston MK, Ressel MW, Seedorff E, Barton MD (eds) Controversies on the origin of world-class gold deposits. Part I. Carlin-type gold deposits in Nevada. SEG Newsletter 59:11–18
Jutras P, Prichonnet G, McCutcheon S (2003) Alleghanian deformation in the eastern Gaspé Peninsula of Québec, Canada. Geol Soc Amer Bull 115:1538–1551
Kerrich R, Goldfarb RJ, Groves DI, Garwin S (2000) The geodynamics of world-class gold deposits: characteristics, space-time distribution, and origins. SEG Rev 13:501–551
Kesler SE, Fortuna J, Ye Z, Alt JC, Core DP, Zohar P, Borhauer J, Chryssoulis SL (2003) Evaluation of the role of sulfidation in deposition of gold, screamer section of the Betze-Post Carlin-type deposit: Nevada. Econ Geol 98:1137–1157
Kirkwood D, Malo M (1993) Across strike geometry of the Grand Pabos fault zone: evidence for Devonian transpression in the Québec Appalachians. Can J Earth Sci 30:1363–1373
Kübler B (1968) Évaluation quantitative du métamorphisme par la cristallinité de l'illite. Bull Cent Rech Pau 2 :385–397
Kübler B (1984) Les indicateurs des transformations physiques et chimiques dans la diagenèse; température et calorimétrie. In : Lagache M (ed) Thermométrie et barométrie géologiques. Soc Fran Minéral Cristal 2:489–596
Malo M (2001) Late Silurian-Early Devonian tectono-sedimentary history of the Gaspé Belt in the Gaspé Peninsula: from a transtensional Salinic basin to an Acadian foreland basin. Bull Can Pet Geol 49:202–216
Malo M, Bourque PA (1993) Timing of the deformation events from Late Ordovician to Mid-Devonian in the Gaspé Peninsula. Geol Soc Amer, Spec Pap 275:101–122
Malo M, Kirkwood D (1995) Faulting and progressive strain history of the Gaspé Peninsula in post-Taconian time: a review. Geol Assoc Can, Spec Pap 41:267–282
Malo M, Moritz R, Roy F, Chagnon A (1993) Géologie et métallogénie du segment est de la faille du Grand Pabos, Gaspésie. Ministère de l'Énergie et des Ressources du Québec, MB 93-551, p 114
Malo M, Tremblay A, Kirkwood D, Cousineau P (1995) Along-strike Acadian structural variations in the Québec Appalachians: consequence of a collision along an irregular margin. Tectonics 14:1327–1338
Malo M, Pelchat C, Dubé B, Chagnon A (1998) Contrasting styles of gold mineralization along the Grand-Pabos-Restigouche fault system: implications for Carlin-like Au-mineralization in the southwestern Gaspé Appalachians. Explor Min Geol 7:217–235
Malo M, Moritz R, Dubé B, Chagnon A, Roy F, Pelchat C (2000) Base metal skarns and Au occurrences in the southern Gaspé Appalachians: distal products of a faulted and displaced magmatic-hydrothermal system along the Grand Pabos-Restigouche fault system. Econ Geol 95:1297–1318
Moritz R, Malo M (1996) Lead isotope signatures of Devonian Acadian structurally-controlled mineral occurrences in Gaspé Peninsula, Québec Appalachians: constraints on the source rock reservoir. Econ Geol 91:1145–1150
Muntean JL, Cline JS, Johnston MK, Ressel MW, Seedorff E, Barton MD (2004) Controversies on the origin of world-class gold deposits. Part I. Carlin-type gold deposits in Nevada. SEG New 59:1 and 11–18
Nelson C (1990) Comparative geochemistry of jasperoids from Carlin-type gold deposits of the estern United Sates. J Geochem Explor 36:171–195
Nutt CJ, Hofstra AH (2003) Alligator Ridge district, east-central Nevada: Carlin-type gold mineralization at shallow depths. Econ Geol 98:1225–1241
O'Neil JR, Clayton RN, Mayeda TK (1969) Oxygen isotope fractionation in divalent metal carbonates. J Chem Phys 51:5547–5558
Pelchat C (1995) Cadre structural des minéralisations aurifères le long de la faille du Grand Pabos, Gaspésie, Québec. Mémoire de maîtrise, Université Laval, Québec, p 85
Peters SG, Leonardson RW, Ferdock GC, Lauha EA (1997) Breccia types in the Betze orebody, Goldstrike mine, Eureka County, Nevada. In: Vikre P, Thompson TB, K Bettles K, Christensen O, Parratt R (eds) Carlin-type deposits field conference. SEG Guidebook Series 28:87–100
Pouchou JL, Pichoir F (1991) Quantitative analysis of homogeneous or stratified microvolumes applying the model "PAP". In: Heinrich KFJ, Newbury DE (eds) Electron probe quantitation. Plenum, New York, pp 31–75
Poulsen KH (1999a) Carlin-type gold deposits and possible Canadian analogues. New 24th Annual Review of Activities, Brunswick, Minerals and Energy Division. Abstract Volume, pp 39–40
Poulsen KH (1999b) Geological environments for Carlin-type gold deposits in Canada. In: New developments in the geological understanding of some major ore types and environments, with implications for exploration. PDAC, Toronto, pp 155–178
Qing H, Veizer J (1994) Oxygen and carbon isotopic composition of Ordovician brachiopods: implications for coeval seawater. Geochim Cosmochim Acta 58:4429–4442
Rey JP, Kübler B (1983) Identification des micas des séries sédimentaires par diffraction X à partir de la série harmonique (001) des préparations orientées. Schweiz Mineral und Petrogr Mitt 63:13–36
Savard M (1985) Indices minéralisés du sud de la Gaspésie. Ministère de l'Énergie et des Ressources du Québec, ET 83-08, p 92
Schroeter TG, Poulsen H (1996) Carbonate-hosted disseminated Au-Ag. In: Lefebure DV, Hoy T (eds) Selected British Columbia mineral deposit profiles; Volume 2, metallic deposits. British Columbia Energy and Mineral Division, Geological Survey Branch, Open File Report 1996-13:9–12
Sheppard SMF (1986) Characterization and isotopic variations in natural waters. In: Valley JW, Taylor HP, O'Neil JR (eds) Stable isotopes in high temperature geological processes. Rev Miner 16:165–181
Sillitoe RH (2004) Distal-disseminated and Carlin-type gold deposits: are they fundamentally different?. SEG News 59:28–30
Squires GC (2004) Selected epigenetic gold and antimony mineralization in the Exploits subzone and Gander zone: a progress report. Government of Newfoundland and Labrador, Department of Natural Resources Mines Branch, Report of activities 2004, pp 55–58
Swinden HS, Dunsworth SM (1995) Metallogeny, Chapter 9. In: Williams H (ed) The Appalachian/Caledonian orogen: Canada and Greenland. Geology of Canada no. 6: Geological Survey of Canada, pp 681–819
Sylvester AG (1988) Strike-slip faults. Geol Soc Amer Bull 100:1666–1703

Theodore TG (1998) Large distal-disseminated precious-metal deposits, Battle Mountain mining district, Nevada. In: Tosdal RM (ed) Contributions to the gold metallogeny of northern Nevada. U.S. Geological Survey Open File Report 98-338:253–258

Tosdal RM (1999) Overview of Carlin-type gold deposits in the Great Basin, Western USA. New developments in the geological understanding of some major ore types and environments, with implications for exploration. PDAC, Toronto, pp 125–146

Valley JW (1986) Stable isotope geochemistry of metamorphic rocks. In: Valley JW, Taylor HP, O'Neil JR (eds) Stable isotopes in high temperature geological processes, Rev Miner 16:71–74

Wares R (1990) Petrographic analysis of auriferous quartz-stibnite veins, St-André-de-Restigouche, Gaspe, Quebec. Report submitted to Noranda Exploration. Ministère de l'Énergie et des ressources du Québec, Report GM 50165, p 208

Williams-Jones AE (1982) Patapédia: an Appalachian calc-silicate-hosted Cu prospect of porphyry affinity. Can J Earth Sci 19:438–455

Williams-Jones AE, Ferreira DR (1989) Thermal metamorphism and H_2O-CO_2-NaCl immiscibility at Patapédia Québec: evidence from fluid inclusions. Contrib Mineral Petrol 102: 247–254